JOURNAL OF PETROLOGY | VOLUME 52 | NUMBER 4 | PAGES 665–690 | 2011 | doi:10.1093/petrology/egq099

Thermal Evolution of the Lithosphere in a Rift Environment as Inferred from the Geochemistry of Mantle Cumulates, Northern Victoria Land, Antarctica

CRISTINA PERINELLI[1]*, PIETRO ARMIENTI[1] AND LUIGI DALLAI[2]

[1]DIPARTIMENTO DI SCIENZE DELLA TERRA, UNIVERSITÀ DEGLI STUDI DI PISA, VIA S. MARIA 53, 56126 PISA, ITALY
[2]ISTITUTO DI GEOSCIENZE E GEORISORSE (IGG-CNR), VIA MORUZZI 1, 56124 PISA, ITALY

RECEIVED JULY 20, 2010; ACCEPTED DECEMBER 27, 2010
ADVANCE ACCESS PUBLICATION FEBRUARY 2, 2011

Among the abundant mantle xenoliths carried by the Cenozoic alkaline basalts of northern Victoria Land, Antarctica, we have studied a suite of clinopyroxene-rich cumulates collected at Browning Pass (Mt. Melbourne Volcanic Province), ranging in composition from wehrlites to clinopyroxenites. Clinopyroxenes belonging to both the Cr-diopside (wehrlites) and Al-augite series (ol-clinopyroxenites and clinopyroxenites) all show convex-upward REE patterns. Modal and cryptic metasomatism has variably affected the xenoliths, accounting for amphibole replacement of clinopyroxene and/or selective enrichment in incompatible elements. Chemical features, along with O–Sr–Nd isotopic data, indicate that both the parental magmas and the metasomatizing melts are related to the Cenozoic magmatic activity and imply the role of at least two mantle components with distinct isotopic fingerprints. The positive covariation between $\delta^{18}O_{olivine}$ and the amount of modal olivine, and between $\delta^{18}O_{olivine}$ and olivine Fo content, suggest that during the fractionation of olivine and pyroxene, the parent magma experienced a change in O-isotope composition; a low-$\delta^{18}O$ melt component was not only added to the minerals during the metasomatic event but was also involved in the genesis of the parental melts. The Browning Pass cumulates are used to constrain the origin of the Antarctic Cenozoic magmatism from a heterogeneous mantle source whose depleted end-member is inferred to be the local lithospheric mantle, whereas the enriched end-member is represented by early metasomatic veins or domains emplaced into the depleted mantle during an amagmatic phase of rifting at the beginning of Ross Sea opening. Thermobarometric analysis of the process shows that the respective contribution to magma generation of the two end-members is related to the change of local thermal regime induced by an 'edge effect' in the mantle circulation at the lithospheric step between the thick East Antarctic craton and the thinned Ross Sea crust.

KEY WORDS: *cumulate xenoliths; lithospheric mantle geochemistry; thermal evolution; northern Victoria Land; Antarctica*

INTRODUCTION

Ultramafic cumulates originating from high-pressure crystal-segregation from melts migrating through mantle conduits and/or crystallized in magma chambers (Wilshire & Shervais, 1975; Frey, 1980; Irving, 1980; Bodinier *et al.*, 1987*a*, 1987*b*; Suen & Frey, 1987; Ho *et al.*, 2000), provide important information about the crystallization conditions of basaltic magmas at mantle depths. Pyroxenites and wehrlites, associated with peridotite xenoliths, are commonly enclosed within the alkaline basic lavas of the McMurdo Volcanic Group (MMVG) in the Ross Sea region of Antarctica, an area of continuing continental rifting where alkaline magmatism has been active since the Early Cenozoic (Fig. 1). The magmatism has been related to a transtensive tectonic regime based on

*Corresponding author. Telephone: +39 050 2215708. Fax: +39 050 2215800. E-mail: cperinelli@dst.unipi.it

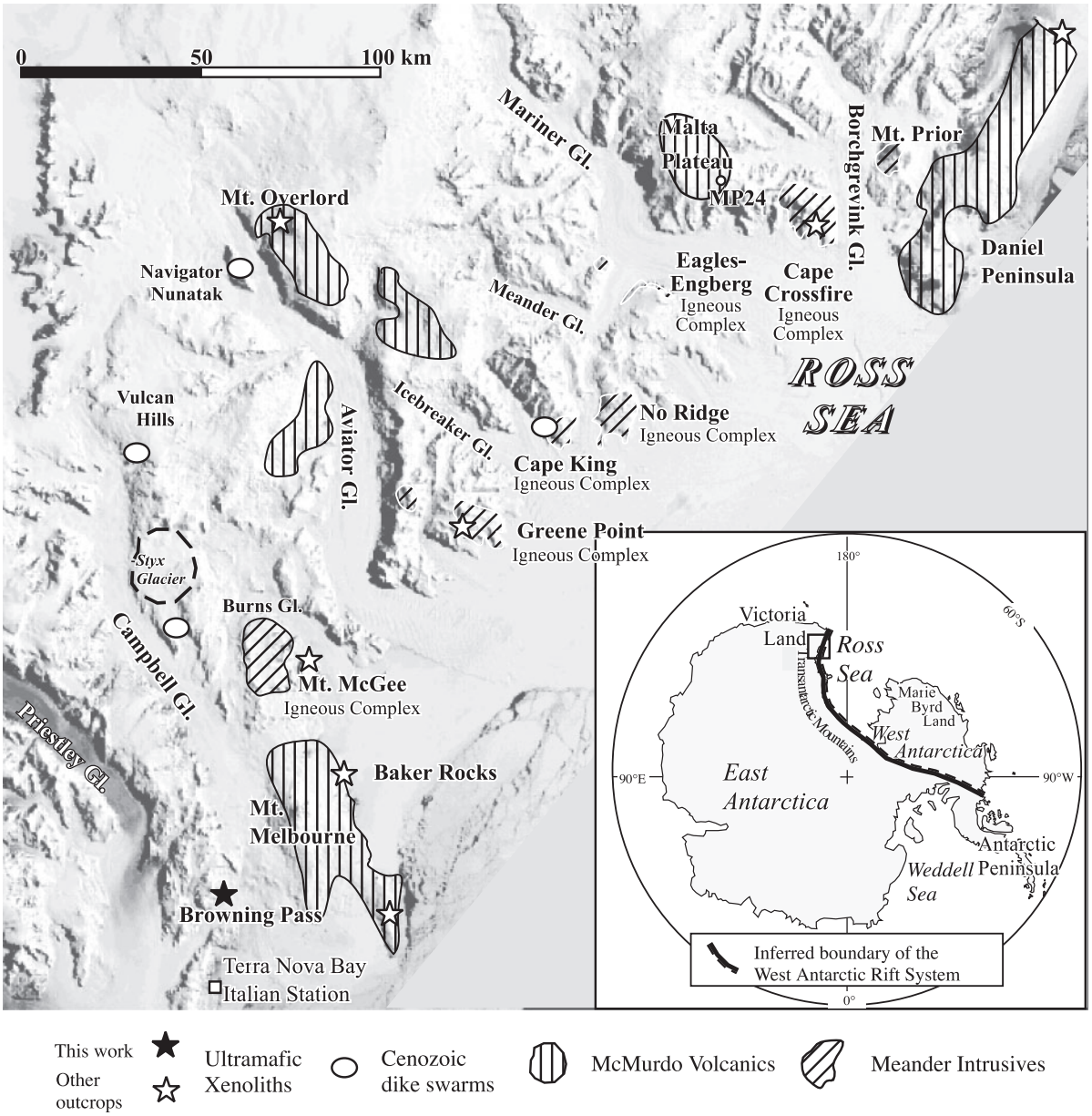

Fig. 1. Map of northern Victoria Land showing the location of Browning Pass and other sampling localities. Inset shows the location of northern Victoria Land within Antarctica.

geothermobarometric estimates (Perinelli *et al.*, 2006; Armienti & Perinelli, 2010).

Detailed studies of spinel peridotite xenoliths from different areas of northern Victoria Land (NVL) have revealed the heterogeneous nature of the upper mantle in this area, resulting from the combined effects of partial melting and metasomatic enrichment processes (Beccaluva *et al.*, 1991; Hornig *et al.*, 1991; Zipfel & Wörner, 1992; Coltorti *et al.*, 2004; Perinelli *et al.*, 2006). In particular, a relationship has been suggested between the most recent metasomatic event recorded by the peridotite xenoliths and the Cenozoic magmatism (Coltorti *et al.*, 2004; Perinelli *et al.*, 2006).

In this study, we present new geochemical and isotopic data for ultramafic pyroxenite and wehrlite xenoliths collected from Browning Pass in the Mt Melbourne Volcanic Province (MMVP) and discuss their origin in the context of the petrogenesis of the basic alkaline magmas of the McMurdo Volcanic Group (MMVG), to gain information on magma differentiation processes in the lithosphere beneath northern Victoria Land. Thermobarometric estimates, obtained using a modification of the

Putirka *et al.* (2003) thermobarometer for application to mantle cumulates, have been used to describe the evolving thermal regime of the local mantle.

GEOLOGICAL SETTING

The Cenozoic volcanic activity of the MMVG is related to the West Antarctic Rift System (WARS, Tessensohn & Wörner, 1991), a region of lithospheric thinning marked by a topographic trough running from the Antarctic Peninsula to the Ross Embayment–northern Victoria Land (Fig. 1) (LeMasurier & Thomson, 1990; Behrendt *et al.*, 1991, 1992). The eastern flank of the rift in northern Victoria Land is the backbone of the Transantarctic Mountains, which represent the uplifted roots of the Early Palaeozoic Ross Orogen. The uplift of the Transantarctic Mountains was practically amagmatic and was accompanied by extensional tectonics in the adjacent Ross Sea region during the Late Cretaceous (e.g. Stagg & Willcox, 1992; Fitzgerald, 1994; Fitzgerald & Stump, 1997; Chand *et al.*, 2001).

Diffuse igneous activity has characterized the WARS since the Eocene. In northern Victoria Land, plutons, dyke swarms and volcanic complexes were emplaced in an area of about 400 km × 80 km (Fitzgerald & Stump, 1997; Tonarini *et al.*, 1997; Rocchi *et al.*, 2002). The volcanic products are grouped collectively as the MMVG (Kyle, 1990), whereas the intrusive–subvolcanic rock types are collectively referred to as the Meander Intrusive Group (Muller *et al.*, 1991; Tonarini *et al.*, 1997). Mantle xenoliths were brought to the surface by primitive alkaline magmas (melanephelinite, basanite and alkali olivine basalt), that erupted from monogenetic cinder cones on the flanks of larger volcanoes or were distributed within the crystalline basement, where the major active faults provided direct magma pathways to the surface (Orlando *et al.*, 1997; Salvini *et al.*, 1997).

SAMPLE DESCRIPTIONS

The cumulate xenoliths are sub-rounded and range from 5 to 20 cm in size. The dominant mineralogy is clinopyroxene + olivine ± spinel; based on modal compositions, the xenoliths have been classified as wehrlites, olivine-clinopyroxenites and clinopyroxenites (Table 1). They prevalently belong to Group II of Frey & Prinz (1978);

Table 1: Modes for cumulate xenoliths from Browning Pass (vol. %)

Sample	Rock	Ol	Cpx	Opx	Sp	Amph	Plg	Glass	Rhön	Texture (Pike & Schwarzman, 1977)
BRP1	OC	9	80		10		1	tr.		Allotriomorphic-granular
BRP2	OC	20	70		10			tr.	tr.	Homogranular
BRP3	Wh	70	25		tr.	tr.		5		Igneous
BRP4	OC	30	70		tr.			tr.		Allotriomorphic-granular
BRP5	Wh	45	55		tr.			tr.		Porphyroclastic
BRP6	C	10	90		tr.	tr.	tr.	tr.		Allotriomorphic-granular
BRP7	C	3	90		7		tr.	tr.	tr.	Allotriomorphic-granular
BRP8	OC	20	78		1		1	tr.		Allotriomorphic-granular
BRP9	C	10	86		2	tr.	1	tr.	tr.	Igneous
BRP10	OC	15	85		tr.			tr.		Allotriomorphic-granular
BRP12	OC	27	70					3		Allotriomorphic-granular
BRP13	OC	39	60		tr.			1		Igneous
BRP14	Wh	60	40		tr.			tr.		Allotriomorphic-granular
BRP16	OC	30	69		tr.			1		Allotriomorphic-granular
BRP17	C	5	77		14	tr.	2	1	tr.	Allotriomorphic-granular
BRP18	Wh	70	22		3		1	4		Igneous
BRP19	Wh	50	50		tr.			tr.		Allotriomorphic-granular
BRP20	Wh	60	40		tr.			tr.		Allotriomorphic-granular
BRP21	C	5	90		2	tr.	1	2	tr.	Igneous
BRP22	C	5	95		tr.		tr.	tr.		Igneous
BRP23	C	7	88		tr.	tr.	1	tr.	tr.	Igneous

Modal compositions were determined by counting at least 1500 points from thin sections. Ol, olivine; Cpx, clinopyroxene; Opx, orthopyroxene; Sp, spinel; Amph, amphibole; Rhön, rhönite; OC, olivine-clinopyroxenite; Wh, wehrlite; C, clinopyroxenite; tr., trace.

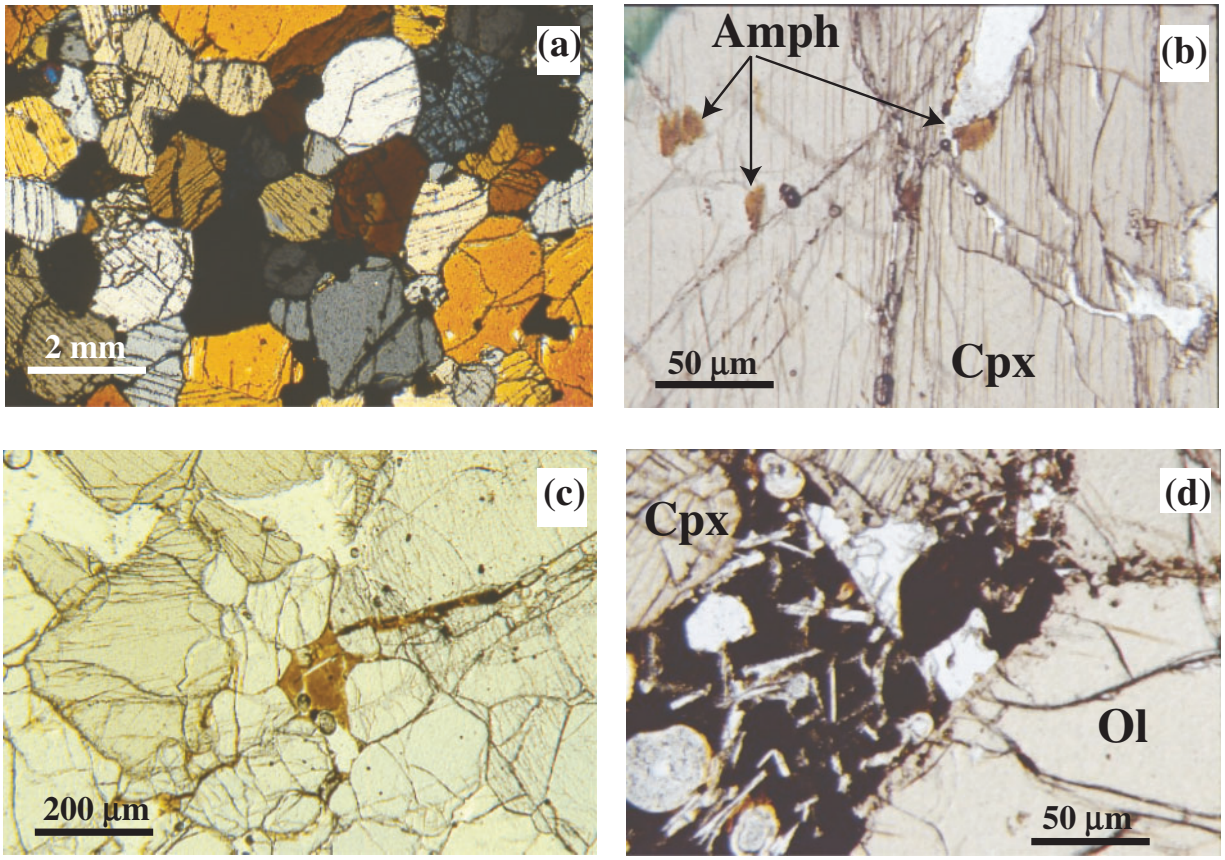

Fig. 2. Photomicrographs of cumulate xenoliths from Browning Pass: (a) typical cumulate texture (crossed polars); (b) amphibole replacements of clinopyroxene in the BRP21 sample (plane-polarized light; ppl); (c) melt-filled interstice surrounded by olivine grains (ppl); (d) glass patches containing plagioclase ± clinopyroxene ± olivine microcrysts (ppl). Amph, amphibole; Cpx, clinopyroxene; Ol, olivine.

only a few wehrlites with Cr-rich diopside fall in Group I of Frey & Prinz (1978). The texture of most of the xenoliths (Fig. 2) is coarse-grained or igneous, with poikilitic clinopyroxene surrounding olivine grains (e.g. BRP3); porphyroclastic textured varieties are rare.

Coarse olivine and clinopyroxene vary in grain size from 1 to 4 mm; however, a few clinopyroxenites contain clinopyroxene megacrysts up to 10 mm long (e.g. BRP22). Although optical observations do not reveal any obvious core–rim zoning in either coarse or poikilitic clinopyroxenes, sometimes they exhibit signs of partial melting and develop narrow 'spongy' or cloudy rims. These secondary features are occasionally accompanied by amphibole replacement (e.g. BRP21; Fig. 2b). Spinel is generally dark brown or opaque, anhedral and sparsely distributed except in BRP19 where it is enclosed in olivine; in rare cases coronas of fine-grained ilmenite needles replace 'primary' spinels. Very scarce accessory plagioclase may occur as an interstitial phase.

Dark brown or pale yellow intergranular glass patches are common (Fig. 2): sometimes these are connected by cracks or by thin crystal boundary channels. The glass patches often contain microcrystalline assemblages of clinopyroxene + olivine ± spinel ± plagioclase; rarely rhönite joins this microcrystalline assemblage. The occurrence of vesicles in these glasses indicates exsolution of a gas phase.

ANALYTICAL TECHNIQUES

Whole-rock major element and Ba, Co, Cr, light rare earth elements (LREE; La and Ce), Ni, Rb, Sr V, Y and Zr contents of a selection of samples were determined by X-ray fluorescence (XRF) spectrometry using a Philips PW 1480 system at the Dipartimento di Scienze della Terra, University of Pisa, using fused disks prepared from a 1:5 sample–lithium tetraborate mixture. Mineral and glass major element compositions were determined by electron microprobe at CNR-IGG, Istituto Geoscienze e Georisorse, Rome, operated at 15 kV accelerating voltage and 30 nA beam current. Counting times were 100 s. To reduce alkali loss during glass analysis we decreased the counting time to 20 s and the beam was defocused to 15 μm. A ZAF correction was applied to all data.

Trace element abundances in minerals and intergranular glasses were determined by secondary ion mass spectrometry (SIMS) at CNR-Istituto Geoscienze e Georisorse of Pavia, on polished sections. Analytical procedures followed those described by Wulff-Pedersen *et al.* (1999).

Oxygen isotope compositions of olivine and clinopyroxene separates were measured at the CNR-Istituto Geoscienze e Georisorse of Pisa by conventional laser fluorination (Sharp, 1995). To measure the oxygen isotope composition of each phase, 1–1·5 mg aliquots of 0·5–1·0 mm olivine and clinopyroxene were taken and laser fluorinated. A 25 W CO_2 laser, operating at a wavelength of 10·6 μm, was used to irradiate the samples placed in a 3 mm diameter hole, within a 32-hole nickel sample plug. Pure fluorine desorbed at 290–310°C from hexafluoropotassium-nickelate salt (Asprey, 1976) and stored in an F_2 reservoir was used as reagent. The O_2 produced during laser fluorination was purified from excess fluorine by means of a KCl trap held at 180°C, and the chlorine was trapped cryogenically. The gas was then transferred to a 13 Å molecular sieve-filled cold finger and analyzed for its oxygen isotope composition using a Finnigan Delta Plus mass spectrometer. On each day of analysis, normally 4–7 aliquots of internal laboratory quartz standards were analyzed, with an average reproducibility of ±0·14‰ (1σ). All samples were analyzed in duplicate, with an analytical precision of ±0·16‰ (1σ) or better. No data correction is necessary for the results, which are reported in the standard per mil (‰) notation. During the period of this study 11 aliquots of the NBS-28 quartz standard were measured, yielding an average value of 9·54 ± 0·17‰ (certified value is 9·60‰). All $\delta^{18}O$ values are reported relative to VSMOW. Because O_2 was the analyte, and was transferred to the IR mass spectrometer via cryogenic trapping on a molecular sieve and subsequent volume expansion (Sharp, 1995), the quantitative yield was monitored empirically by comparing the P_{O2} gas in the IR mass spectrometer bellow all-way-open produced by each reacted mineral versus the sample weight of the sample. Phases of the same kind should plot along a straight line; that is, the best-fit line defined by the same phases of known values measured in the same laboratory.

The Sr–Nd isotope compositions of clinopyroxenes were determined at CNR-Istituto Geoscienze e Georisorse of Pisa using a conventional ion exchange method and a Finnigan MAT 262 multicollector mass spectrometer. $^{87}Sr/^{86}Sr$ ratios were normalized to $^{86}Sr/^{88}Sr = 0{\cdot}1194$ and $^{143}Nd/^{144}Nd$ to $^{146}Nd/^{144}Nd = 0{\cdot}7219$. Replicate measurements of NBS 987 (NIST SRM 987) and J Nd i-1 (La Jolla) standards gave values of $^{87}Sr/^{86}Sr = 0{\cdot}710252 \pm 0{\cdot}000011$ and $^{143}Nd/^{144}Nd = 0{\cdot}512100 \pm 0{\cdot}00007$, respectively.

XENOLITH BULK-ROCK CHEMISTRY

Major and trace element compositions of representative samples are given in Table 2. They show a wide range in composition that reflects variations in the modal proportions of the minerals. The Mg-number value [MgO/(MgO + FeO_{tot}) molar] ranges between 0·72 and 0·84 and is negatively correlated with the CaO, Al_2O_3 and TiO_2 contents and with the modal abundance of clinopyroxene (Table 2).

Compatible trace elements abundances, Ni (393–1714 ppm) and Cr (502–1719 ppm), vary depending on the modal proportion of olivine (Tables 1 and 2) whereas the content of incompatible trace elements is related to the variation in clinopyroxene modal abundance as well as to the occurrence of glass patches.

MINERAL AND GLASS CHEMISTRY

Major elements

Major element composition data for the minerals in the cumulate xenoliths are presented in Tables 3–7. Clinopyroxene and olivine grains have a uniform composition in each sample. Chemical zoning within crystals is limited to clinopyroxenes with spongy rims or next to glass patches and is restricted to the outer part of grains (maximum 100 μm wide); spinels exhibit a greater degree of compositional heterogeneity.

Olivine

Olivine Fo content varies widely between samples (from 74·8 to 83·6, Table 3). NiO abundance varies from below detection limit to 0·43 wt % and is positively correlated with Fo. The CaO content ranges between 0·10 and 0·28 and does not exhibit any correlation with Fo. Microcrystals in glass pods exhibit higher CaO contents (0·34–0·47 wt %) and their Fo contents are in the range Fo 72·4–Fo 80·5 (Table 3).

Clinopyroxene

Clinopyroxene compositions vary from augite to diopside (Wo40–50, En50–37 and Fs10–13) with Mg-number between 0·72 and 0·83 (Table 4). Most have compositions similar to the clinopyroxenes of Group II of Frey & Prinz (1978), with low MgO (<15 wt %) and Cr_2O_3 (<0·5 wt %) contents; clinopyroxenes in wehrlites have compositions similar to Group I clinopyroxenes of Frey & Prinz (1978) with MgO >15 wt % and Cr_2O_3 ≥1 wt %. The spread of Al_2O_3 and TiO_2 contents is wide (5·0–8·9 wt % and 0·84–2·24 wt %, respectively) and is negatively correlated with Mg-number (Fig. 3); a weak negative near-linear trend can also be seen on the Mg-number vs Na variation plot. In contrast, Mg-number is positively correlated with

Table 2: Major and trace element compositions of representative cumulate xenoliths from Browning Pass and their host lava; the composition of the host lava is also reported

	BRP3 Wh	BRP5 Wh	BRP14 Wh	BRP16 OC	BRP23 C	Host lava BRP (MB65b)
SiO_2	43·31	43·84	42·01	42·98	43·29	43·91
TiO_2	0·26	0·73	0·78	1·4	1·83	2·76
Al_2O_3	1·63	4·47	3·82	5·8	7·14	14·30
FeO_t	11·88	11·92	12·26	13·64	12·19	12·36
MnO	0·12	0·18	0·21	0·2	0·18	0·20
MgO	36·18	27·95	28·37	20·76	17·56	10·30
CaO	5·64	9·58	9·04	13·51	16·01	9·04
Na_2O	0·14	0·44	0·39	0·58	0·64	2·85
K_2O	0·01	0·05	0·04	0·04	0·03	1·11
P_2O_5	0·02	0·03	0·04	0·03	0·02	0·53
LOI	0·65	0·62	0·84	0·66	0·62	2·20
Mg-no.	0·84	0·81	0·80	0·73	0·72	0·60
V	133	192	155	265	347	163
Cr	1678	1719	1599	1169	502	454
Co	102	98	112	88	79	60
Ni	1714	1051	751	461	393	279
Rb	4	5	4	6	5	28·28
Sr	48	49	56	73	78	684
Y	10	14	13	19	26	26·26
Zr	18	29	37	54	61	262
Nb						67·87
Ba	8	16	17	10	11	387
La	3	1	1	2	2	40·20
Ce	10	12	7	20	23	84·37
Pr						10·38
Nd						40·34
Sm						8·16
Eu						2·67
Gd						8·14
Tb						1·05
Dy						5·81
Ho						0·97
Er						2·60
Tm						0·32
Yb						2·10
Lu						0·27
Hf						5·33
Ta						3·52
Th						4·66
U						1·33

OC, olivine-clinopyroxenite; Wh, wehrlite; C, clinopyroxenite. Mg-number = [MgO/(MgO + FeO_{tot}) molar]. LOI, loss on ignition.

SiO_2 (not shown) and Cr. With respect to the core, the rims of the spongy crystals are complementary; richer in TiO_2 and poorer in Na_2O (Table 4, Fig. 3). Clinopyroxenes crystallized in the glass pockets are in general enriched in the Wo component; their TiO_2 and Na_2O contents overlap those of the rims of the spongy crystals. No clear correlations are found between the variation of major oxides and Mg-number (Table 4).

Spinel

This phase displays a very wide variation of composition (Table 5): the Mg-number [=Mg/(Mg + Fe^{2+}) atomic] ranges from 0·22 to 0·61 and the Al_2O_3 contents vary between 10·5 and 56·9 wt %, with a positive correlation (Fig. 4a). The Cr_2O_3 content is low (<11 wt %), except for the spinels in the wehrlites, for which the Cr_2O_3 content is ~30 wt % (BRP19). The ratio [Fe^{3+}/(Fe^{3+} + Al + Cr)] ranges from 0·09 to 0·54 and is negatively correlated with Mg-number but positively correlated with TiO_2 (Fig. 4b and c). Such trends overlap the evolution of spinel composition during fractional crystallization of olivine and pyroxene from a basic magma (Fe–Ti trend of Barnes & Roeder, 2001). Spinels with low [Fe^{3+}/(Fe^{3+} + Al + Cr)] ratios and high Mg-number resemble those of Group II of Frey & Prinz (1978); similar spinel compositions were found in pyroxenites sampled from other areas of northern Victoria Land (Gamble & Kyle, 1987; Gamble *et al.*, 1988). Spinels with high [Fe^{3+}/(Fe^{3+} + Al + Cr)] ratios, low Mg-number (Fig. 4) and the highest TiO_2 contents (>16 wt %) are in general associated with the occurrence of glass (BRP21 and BRP22).

Glass

Intergranular glass encompasses a wide compositional range in the alkaline field (Table 6; Fig. 5). The SiO_2 content is between 47 and 52 wt %; Mg-number varies between 0·31 and 0·48 but no clear correlation is recognizable. A negative correlation is observed between FeO_{tot} and SiO_2 (not shown). Na_2O is always higher in concentration than K_2O ($K_2O/Na_2O = 0·33–0·66$). In general, the glasses have low analytical totals that, together with the vesicularity (Fig. 2d), suggest that the melts were volatile rich.

When plotted in the basalt tetrahedron CaTs–Di–Ol–Q of the CMAS system (projection from the diopside component, Fig. 5), the glasses reveal their similarity to the primitive lavas of northern Victoria Land; however, the higher SiO_2 contents in the glasses do not correlate with the variations of the other major element oxides, as expected for differentiation products of intercumulus liquids. We have suggested previously that this indicates a reaction relationship with the host cumulate (Perinelli *et al.*, 2008) and that the glasses are a result of metasomatism induced by alkaline melts similar to those feeding the Cenozoic magmatism of northern Victoria Land (NVL). A detailed

Table 3: Representative analyses of olivines

	BRP1	BRP 3	BRP 7	BRP 8	BRP 12	BRP 19	BRP 20	BRP 21	BRP 22
SiO_2	38·80	40·28	38·54	38·74	39·03	39·99	39·67	38·43	38·58
FeO	21·88	15·36	24·62	21·81	18·50	16·39	15·88	23·20	23·15
MnO	0·25	0·16	0·31	0·32	0·30	0·22	0·13	0·14	0·27
MgO	38·61	44·08	37·11	39·67	41·65	43·59	43·91	38·34	38·56
NiO	0·08	0·43		0·10	0·28	0·33	0·38		
CaO	0·19	0·28	0·38	0·27	0·20	0·16	0·19	0·28	0·10
Total	99·81	100·58	100·96	100·90	99·96	100·67	100·16	100·39	100·66
Fo	75·9	83·6	72·9	76·4	80·0	82·6	83·1	74·7	74·8

	BRP1*	BRP 12*	BRP 12*	BRP 21*
SiO_2	38·98	38·18	38·94	39·45
FeO	23·34	22·88	24·29	18·19
MnO	0·43	0·53	0·36	0·20
MgO	36·33	37·84	35·70	42·15
NiO				0·31
CaO	0·45	0·47	0·34	0·36
Total	99·53	99·89	99·63	100·66
Fo	73·5	74·7	72·4	80·5

*Olivine crystallized in glass patches.
Fo, fosterite component.

discussion of the metasomatic events affecting the NVL mantle, based on intergranular glass inclusions, has been given by Perinelli *et al.* (2008).

Other phases

Plagioclase compositions range between An67 and An75 (Table 7). These crystals are interstitial and do not show any zoning. The composition of microlites in the glass pods ranges from An48 to An68.

The amphibole replacing clinopyroxene (BRP21 and BRP22) is kaersutite [classified according to Leake *et al.* (1997)]. Its Mg-number values (~0·71) are rather uniform; however, BRP21 amphiboles are slightly richer in Al_2O_3, MgO and K_2O, whereas their Cr_2O_3 content is lower (Table 7). The composition of these amphiboles is close to that of amphiboles found in pyroxenite samples from northern Victoria Land (Gamble & Kyle, 1987; Gamble *et al.*, 1988; Beccaluva *et al.*, 1991; Hornig *et al.*, 1991; Coltorti *et al.*, 2004).

Euhedral rhönite crystals are usually associated with glass pods (Table 7). Their composition is comparable with those recorded by Gamble & Kyle (1987) in the wehrlites from Foster Crater (McMurdo Sound area).

Trace elements

Clinopyroxene

Clinopyroxenes are, in general, chemically uniform with respect to trace elements (Table 8). Intra-mineral zoning in highly incompatible elements was found in those clinopyroxenes with spongy rims (BRP8 and BRP12; Fig. 6) and appears to be limited to within 200–300 μm of the crystal boundary.

On primitive mantle normalized diagrams, (McDonough & Sun, 1995), the incompatible element patterns are similar but show differences in the degree of enrichment as evidenced by the variation in the depth of the Sr, Zr and Ti anomalies with respect to the adjacent REE (Fig. 6a). The chondrite-normalized REE patterns (Fig. 6b) have a convex-upward shape similar to those of clinopyroxenes in pyroxenites crystallized from alkali basalts (Wilshire & Shervais, 1975; Frey & Prinz, 1978; Suen & Frey, 1987). With the exception of BRP21, the REE profiles are comparable and show an increase of REE abundance from wehrlites to ol-clinopyroxenites (ΣREE_{core} 23–45 ppm; Fig. 6b). BRP21 clinopyroxenes display a less pronounced convex-upward profile and have the highest $(Ce/Sm)_N$ ratios (>1).

Table 4: Representative analyses of clinopyroxenes

	BRP1	BRP3	BRP7 core	BRP7 Py rim	BRP8 core	BRP8 Py rim	BRP12 core	BRP12 Py rim	BRP19 core	BRP20 core
SiO_2	47·34	51·02	47·65	45·87	49·53	49·32	48·99	47·63	51·18	50·86
TiO_2	2·12	0·91	2·24	3·34	1·25	1·65	1·14	2·46	0·84	0·94
Al_2O_3	8·92	5·01	8·67	7·24	7·34	5·53	7·80	5·82	4·39	4·72
FeO_{tot}	8·01	5·72	7·50	7·45	6·54	7·12	5·83	6·83	6·25	6·18
MnO	0·11	0·09	0·07	0·06	0·17	0·11	0·09	0·11	0·16	0·10
MgO	12·18	15·69	12·64	12·34	14·64	13·88	14·07	13·63	16·12	15·77
CaO	19·54	20·23	20·51	22·90	19·40	21·22	20·95	22·78	18·97	19·45
Na_2O	0·79	0·53	0·78	0·39	0·68	0·40	0·52	0·46	0·69	0·55
Cr_2O_3		0·98	0·07	0·00	0·31	0·38	0·02		0·99	1·09
Total	99·00	100·19	100·11	99·59	99·87	99·61	99·41	99·73	99·59	99·66
Wo	45·62	43·40	46·61	49·86	43·10	45·96	46·40	48·38	39·91	42·01
En	39·58	46·86	39·97	37·37	45·26	41·82	43·36	40·29	49·45	47·40
Fs	14·80	9·74	13·42	12·77	11·64	12·22	10·24	11·33	10·63	10·59
Mg-no.	0·73	0·83	0·75	0·75	0·80	0·78	0·81	0·78	0·82	0·82

					Clinopyroxenes in glass patches				
	BRP21 core	BRP21 Py rim	BRP 21*	BRP22	BRP 1	BRP 3	BRP 7	BRP12	BRP15
SiO_2	47·07	47·43	47·57	49·97	46·05	48·84	46·35	48·05	49·79
TiO_2	2·06	2·22	2·00	1·49	3·04	2·56	3·51	3·48	2·44
Al_2O_3	8·41	8·96	8·84	6·55	9·92	6·08	7·82	6·87	5·02
FeO_{tot}	7·20	7·86	7·18	6·90	7·46	6·89	7·58	6·89	5·52
MnO	0·11	0·10	0·10	0·12	0·07	0·06	0·10	0·12	0·07
MgO	12·73	11·52	12·87	13·87	11·27	12·99	12·27	12·74	15·07
CaO	20·34	21·24	20·53	20·42	22·53	22·24	23·08	22·37	22·34
Na_2O	0·71	0·68	0·76	0·70	0·36	0·45	0·42	0·47	0·47
Cr_2O_3	0·23	0·25	0·22	0·24	0·02	0·28		0·01	0·18
Total	98·86	100·25	100·07	100·27	100·72	100·40	101·13	101·00	100·90
Wo	46·48	48·85	46·53	45·16	51·10	48·62	50·01	49·09	48·85
En	40·47	36·86	40·59	42·70	35·56	39·51	37·00	38·90	36·86
Fs	13·04	14·29	12·88	12·14	13·34	11·86	12·99	12·01	14·29
Mg-no.	0·76	0·72	0·76	0·78	0·73	0·77	0·74	0·77	0·83

Mg-number = [Mg/(Mg + Fe_{tot}) molar]; Py, pyrometamorphic; Wo–En–Fs, wollastonite–enstatite–ferrosillite clinopyroxene end-members.
*Associate with amphibole.

The trace element compositions of the rims of spongy crystals are characterized by higher REE contents than the core (e.g. in BRP8 the ΣREE is 40 and 68 ppm in the core and rim, respectively) and the Ti negative deflection tends to disappear whereas the variation in Sr content is less marked (Fig. 6a).

Radiogenic and stable isotope compositions

The $^{87}Sr/^{86}Sr$ and $^{143}Nd/^{144}Nd$ compositions of clinopyroxenes and $\delta^{18}O$ values of olivines and clinopyroxenes are listed in Table 9. Clinopyroxenes display a narrow range in isotope composition: $^{87}Sr/^{86}Sr = 0{\cdot}702892–0{\cdot}702955$ and $^{143}Nd/^{144}Nd = 0{\cdot}512937–0{\cdot}512954$. These values are fully

Table 5: Representative analyses of spinels

	BRP 1	BRP 7 core	BRP 7 rim	BRP 8 core	BRP 8 core–rim	BRP 8 rim	BRP 19 core	BRP 19 rim
SiO_2	0·11	0·08	0·02	0·13	0·17	0·14	0·14	0·05
TiO_2	0·89	1·62	1·46	1·36	1·36	14·74	2·23	2·20
Al_2O_3	56·93	55·19	54·94	54·53	54·07	14·63	26·72	27·08
Cr_2O_3	0·48	0·64	0·63	0·42	0·39	0·56	29·38	30·26
FeO_{tot}	26·01	26·50	28·03	28·30	28·43	60·67	28·95	28·79
MnO	0·15	0·00	0·14	0·11	0·20	0·29	0·09	0·10
MgO	15·43	15·97	14·78	15·15	15·37	8·82	12·48	11·52
Total	99·89	99·92	99·98	99·87	99·83	99·70	99·86	99·95
Mg-no.	0·60	0·61	0·57	0·59	0·60	0·31	0·53	0·50
cr-no.	0·01	0·01	0·01	0·01	0·00	0·02	0·42	0·43

	BRP 21 core	BRP 21 reaction rim	BRP 21 reaction rim	BRP 22 core	BRP 22 rim	BRP 22 core	BRP 22 rim
SiO_2	0·19	0·12	0·10	0·13	0·16	0·10	0·08
TiO_2	1·69	16·05	21·44	9·47	16·52	3·02	2·93
Al_2O_3	50·16	12·29	10·35	18·97	11·41	36·79	36·35
Cr_2O_3	3·25	2·99	3·12	10·36	7·43	10·84	10·84
FeO_{tot}	31·60	59·41	57·60	53·14	56·11	38·51	38·84
MnO	0·11	0·36	0·38	0·27	0·30	0·05	0·11
MgO	12·97	8·63	6·91	7·65	8·04	10·69	10·85
Total	99·78	99·72	99·79	99·87	99·81	99·90	99·92
Mg-no.	0·51	0·30	0·22	0·30	0·28	0·44	0·45
cr-no.	0·04	0·14	0·17	0·27	0·30	0·16	0·17

Mg-number = [Mg/(Mg + Fe^{2+}) atom]; Cr- number = [Cr/(Cr + Al) atom].

Table 6: Major element composition of intergranular glasses

	BRP 3	BRP 3	BRP 3	BRP 12	BRP 12	BRP 19	BRP 19	BRP 19
SiO_2	48·34	47·07	50·29	47·10	48·25	49·49	52·09	51·13
TiO_2	3·51	4·81	2·67	3·41	3·46	3·81	3·16	3·57
Al_2O_3	15·81	13·54	18·29	15·61	15·68	15·74	16·23	16·26
FeO_{tot}	10·81	13·43	7·60	9·72	10·04	8·94	6·94	7·24
MnO	0·22	0·21	0·17	0·29	0·15	0·11	0·13	0·10
MgO	2·72	3·90	3·77	3·69	3·61	3·64	3·52	3·81
CaO	6·25	8·28	7·73	8·14	8·27	7·53	6·17	6·81
Na_2O	5·75	4·45	6·44	4·64	4·84	5·77	5·69	5·82
K_2O	3·61	2·69	2·14	3·06	2·99	3·09	3·45	3·22
Total	97·01	98·38	99·10	95·65	97·29	98·12	97·38	97·95
Mg-no.	0·31	0·34	0·47	0·40	0·39	0·42	0·48	0·48
Q								
or	21·36	15·88	12·66	18·08	17·67	18·28	20·41	19·00
ab	15·89	15·43	22·99	13·75	15·62	18·45	27·51	24·20
an	6·67	9·02	14·66	12·74	12·24	7·93	8·53	8·76
ne	17·74	12·05	17·08	13·81	13·72	16·45	11·19	13·56
lc								
di	20·63	27·03	19·64	23·10	24·10	24·45	18·17	20·55
hy								
ol	8·07	9·82	7·00	7·69	7·35	5·33	5·56	5·11
il	6·66	9·13	5·07	6·48	6·58	7·24	6·00	6·78

Mg-number = [MgO/(MgO + FeO_{tot}) molar].

compatible with the compositional range observed for near-primary magmas of the Cenozoic cycle of northern Victoria Land province and, in particular, span the field between the host lava (MB65) and MB32 alkali basalt values (Fig. 7; Nardini *et al.*, 2009) which are younger than 2 Ma (Armienti & Baroni, 1999). However, clinopyroxenes from the amphibole-bearing xenolith BRP21 have lower $^{87}Sr/^{86}Sr$ and $^{143}Nd/^{144}Nd$ ratios than clinopyroxenes in the other xenolith samples (Fig. 7b, Table 9). We are confident that, because of their well-preserved cumulus texture, they are not affected by annealing. All the analysed clinopyroxenes are relatively young and their Sr and Nd isotopic ratios need no age correction. In the worst case an age correction of 50 Ma could produce a variation of four units on the fifth decimal place that lowers the Nd isotopic ratios to the values of the Cenozoic intrusions.

Olivine $\delta^{18}O$ values vary from 5·00 to 5·72‰; they are very close to the range defined by Mattey *et al.* (1994) for olivine from lithospheric mantle peridotites (5·18 ± 0·28‰) and fall in the range determined for olivine of NVL spinel peridotites (4·80–5·81‰; Perinelli *et al.*, 2006) and Cenozoic basalts (4·92–5·53‰; Nardini *et al*, 2009; Fig. 8). Olivine $\delta^{18}O$ values vary in concert with its modal abundance ($R^2 = 0·8$) and a broadly positive correlation is found between $\delta^{18}O$ and Fo content, with high-Fo olivines having higher $\delta^{18}O$ values. Accordingly, olivines in the amphibole-bearing BRP21 sample have the lowest Fo content and the lowest $\delta^{18}O$ value (Fig. 8, Table 9).

Clinopyroxene shows a smaller range of variability in $\delta^{18}O$ values with respect to the coexisting olivine: most values fall in a restricted range from 5·16 to 5·29‰ and only BRP1 and BRP8 have higher values (5·48 and 5·53‰, respectively). On the whole, the values overlap the $\delta^{18}O$ range of megacrysts from alkaline basalts (5·01–6·48‰; Dobosi *et al.*, 1998; Xia *et al.*, 2004) and are comparable with those for clinopyroxenes from NVL spinel-lherzolites and harzburgites (4·96–5·71‰; Perinelli *et al.*, 2006). No apparent correlation was observed between the $\delta^{18}O$ values and the major and trace element composition of the clinopyroxenes.

Table 7: Plagioclase, amphibole, and rhönite analyses

	Plagioclase									
	BRP1	BRP1	BRP3	BRP7	BRP8	BRP8	BRP12	BRP19	BRP21	BRP21
SiO_2	49·68	51·50	54·15	50·84	49·27	53·14	53·78	56·56	50·02	51·57
Al_2O_3	32·03	30·48	28·85	30·65	32·13	29·88	28·53	27·33	31·72	30·86
FeO_{tot}	1·11	0·56	0·51	0·90	0·60	0·80	0·67	0·45	0·88	0·72
MgO	0·14	0·10	0·12	0·09	0·12	0·10	0·08	0·06	0·13	0·11
CaO	15·20	13·73	11·87	12·56	15·45	12·81	11·43	9·96	15·10	13·51
Na_2O	2·66	3·68	4·49	4·79	2·36	4·02	4·72	5·57	2·79	3·52
K_2O	0·14	0·12	0·34	0·43	0·13	0·23	0·58	0·61	0·18	0·31
Total	100·97	100·16	100·32	100·26	100·07	100·98	99·78	100·54	100·82	100·60

	Amphibole				Rhönite			
	BRP21	BRP21	BRP22	BRP22	BRP7	BRP7	BRP21	BRP21
SiO_2	39·86	40·69	40·95	40·88	22·77	23·24	28·01	27·48
TiO_2	5·17	5·54	5·20	5·01	13·57	13·26	11·13	11·70
Al_2O_3	14·14	13·97	13·05	13·25	17·92	17·19	16·17	16·01
FeO_{tot}	10·04	9·86	10·02	9·62	19·16	19·09	14·71	13·70
MnO	0·10	0·10	0·18	0·08	0·16	0·12	0·04	0·09
MgO	12·76	13·33	13·62	13·65	12·99	13·47	17·22	17·86
CaO	11·71	11·57	11·01	11·11	12·73	12·78	10·94	11·72
Na_2O	2·48	2·60	2·74	2·59	0·61	0·78	1·51	1·26
K_2O	0·95	0·89	0·64	0·66				
Cr_2O_3	0·17	0·22	0·47	0·59	0·09	0·06	0·26	0·19
Total	97·21	98·55	97·41	96·85	99·91	99·94	99·74	99·81
Mg-no.	0·69	0·71	0·71	0·72	0·55	0·56	0·68	0·70

Mg-number = [Mg/(Mg + Fe_{tot}) molar].

Oxygen isotope fractionation ($\Delta^{18}O_{cpx-ol}$) between clinopyroxene and olivine ranges between +0·36 and −0·43 (Fig. 9). The expected fractionation of about +0·4‰ for spinel peridotites (Mattey *et al.*, 1994) is observed only in sample BRP8 ($\Delta^{18}O_{cpx-ol}$ = +0·36‰). Values between +0·36 and +0·1‰ have been reported for phenocrysts and megacrysts in basaltic rocks (Dobosi *et al.*, 1998; Baker *et al.*, 2000, and references therein; Xia *et al.*, 2004), and interpreted as resulting from crystallization over a range of temperature between 1000 and 1200°C (Chiba *et al.*, 1989; Kyser, 1990; Zheng, 1993). Three wehrlite samples (BRP3, BRP19 and BRP20) show negative $\Delta^{18}O_{cpx-ol}$ values (−0·43, −0·16 and −0·21‰, respectively) which indicate that the mineral isotopic equilibrium was perturbed, possibly by open-system metasomatic processes (Gregory & Taylor, 1986; Mattey *et al.*, 1994; Chazot *et al.*, 1997; Zhang *et al.*, 2001; Perkins *et al.*, 2006).

DISCUSSION

Nature of cumulates

The microstructures and compositional characteristics of the cumulates suggest that the wehrlites and pyroxenites exhumed by the NVL alkali basalts were formed by a fractional crystallization process. In particular, the studied cumulates probably reflect the P–T conditions of the earliest stages of differentiation of the MMVG magmas. The modal variation from wehrlite to clinopyroxenite, the positive correlation of Mg-number (0·82–0·72) with the modal and major and compatible trace element composition (Ni, Co) of the whole-rocks (Tables 1 and 2), and the variability

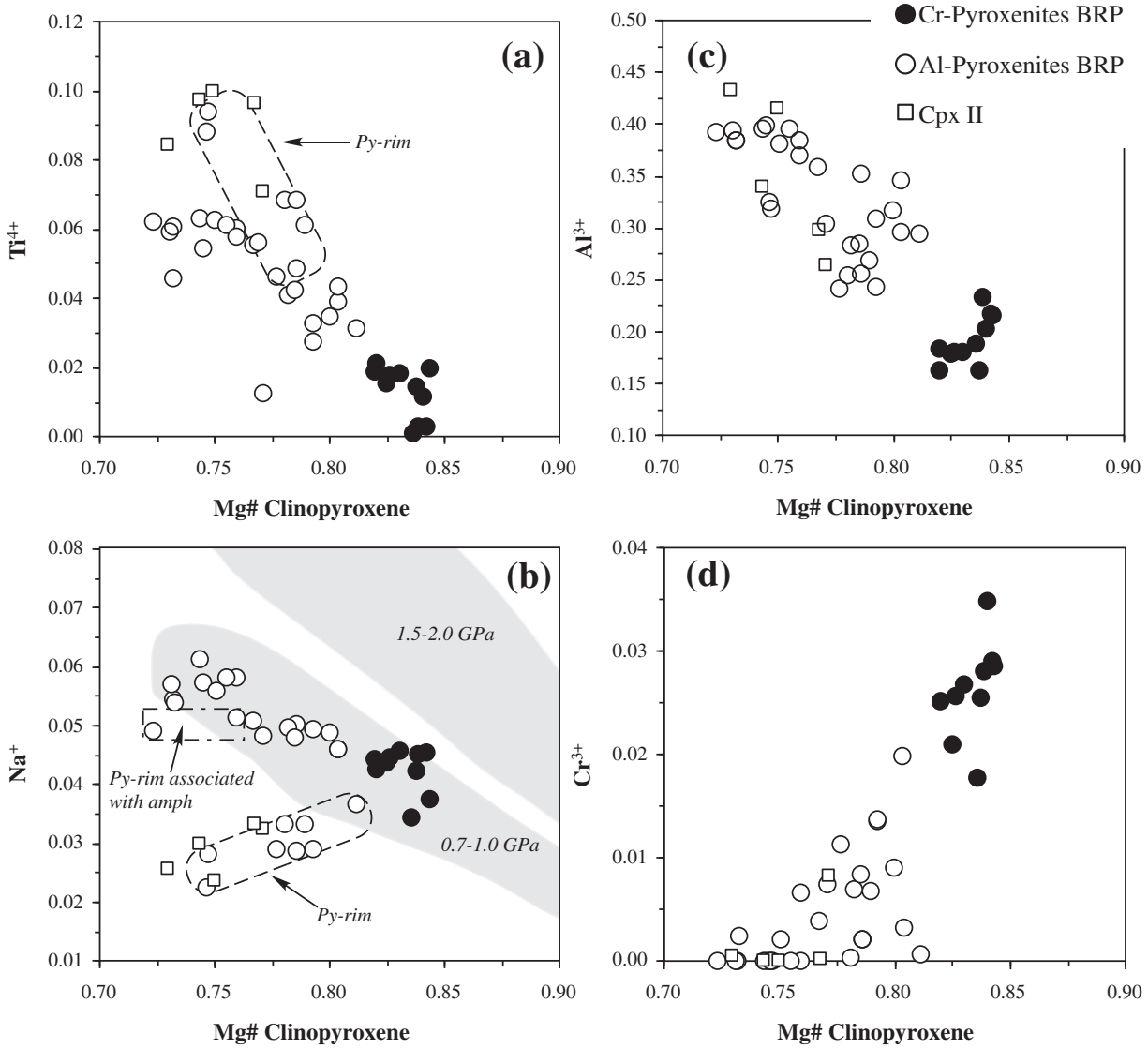

Fig. 3. Compositional variation of Ti^{4+} (a), Na^{+} (b), Al^{3+} (c) and Cr^{3+} (d) vs Mg-number [$(MgO/MgO + FeO_{tot})$ molar] in clinopyroxenes from the Browning Pass xenoliths (cations per formula unit). Shaded fields enclose clinopyroxenes experimentally crystallized from silicate melts at pressures of 0·7–1·0 and 1·5–2·0 GPa (data from LEPR database: http://lepr.ofm-research.org; Adam & Green, 1994; Akinin *et al.*, 2005).

in composition of the dominant phases and the convex-upward shape of REE patterns of clinopyroxenes are all features consistent with a fractional crystallization process from parental mafic liquids at variable pressures and temperatures (Frey & Prinz, 1978; Irving & Frey, 1984).

High-pressure experiments on a natural basanite (0·5–3·0 GPa, 1050–1350°C; Adam & Green, 1994) indicated a negative covariation of the Al^{IV}/Al^{VI} ratio, Ti, Ca, and REE contents of clinopyroxene with Mg-number with increasing presure. The TiO_2 contents of the primary clinopyroxenes of NVL xenoliths vary between 0·5 and 2·3 wt % and show a negative correlation with Mg-number and REE content that might indicate polybaric crystallization from the same melt (Adam & Green, 1994); however, no clear relationship is observed between Mg-number and Al^{IV}/Al^{VI} ratio or Ca. The trend of Mg-number vs Na^{+} (Fig. 3b), parallel to that of experimental clinopyroxenes formed between 0·7 and 1·0 GPa, suggests near-isobaric fractionation of distinct magma batches.

Estimates of parental liquid compositions

The high Mg-number values of olivine and clinopyroxene imply that NVL wehrlites crystallized from high-Mg melts. We can estimate the Mg-number of the parental liquid(s) using the partition coefficient for Fe and Mg

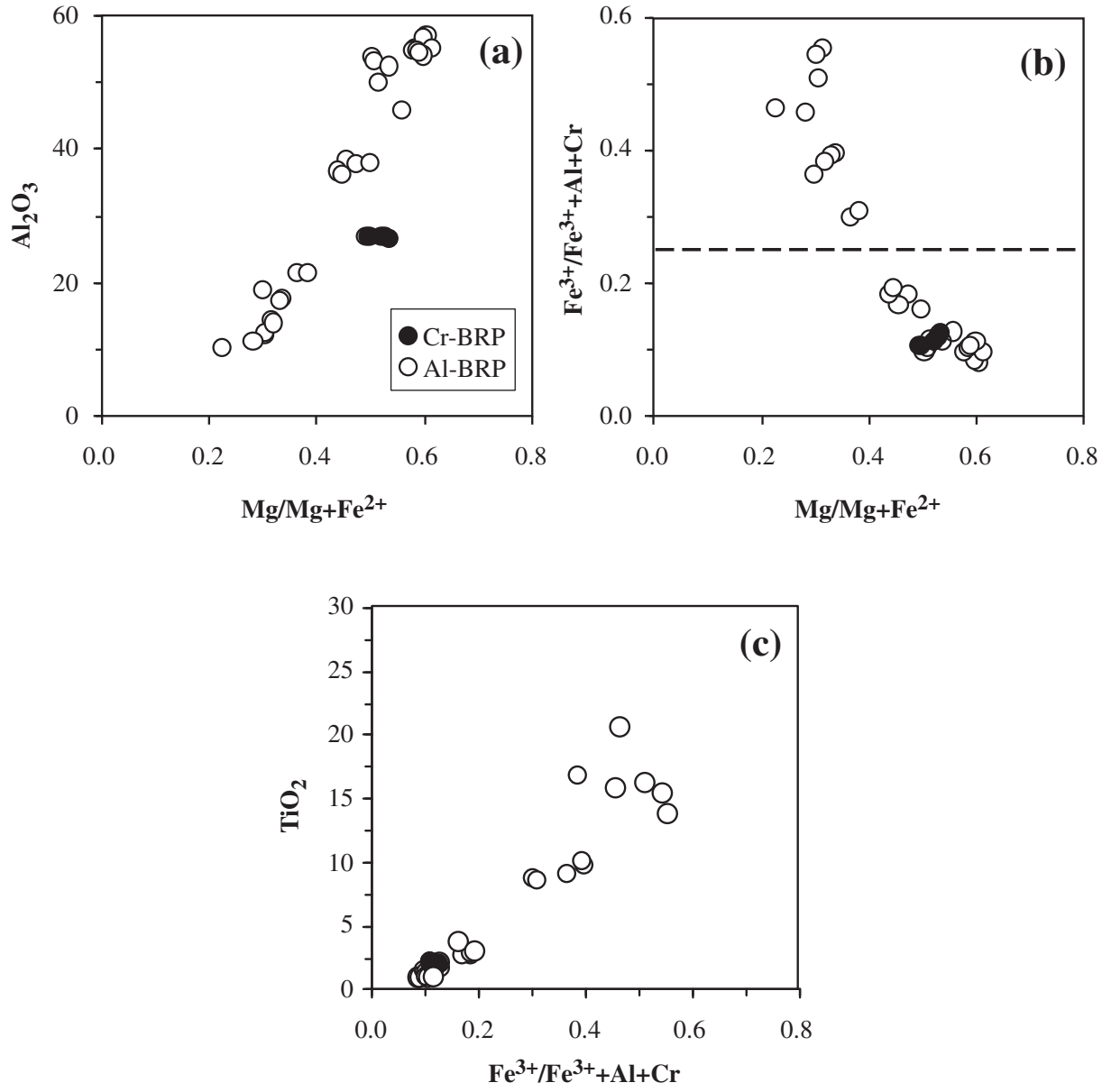

Fig. 4. (a) Variation of spinel Mg-number ($Mg/Mg + Fe^{2+}$) vs Al_2O_3 (wt %). (b) Spinel Mg-number vs $Fe^{3+}/(Fe^{3+} + Al + Cr)$. The dashed line limiting two distinct fields is from Gamble *et al.* (1987). (c) $Fe^{3+}/(Fe^{3+} + Al + Cr)$ vs TiO_2. The data follow the typical Fe–Ti trend (Barners & Roeder, 2001) of spinel compositional variation during fractional crystallization of a basic magma.

between olivine/clinopyroxene and melt ($K_D^{Fe/Mg}$). Assuming a $K_D^{Fe/Mg} = 0 \cdot 3$ for olivine (Roeder & Emslie, 1970) and 0·28 for clinopyroxene (Putirka *et al.*, 2003), the wehrlites would have equilibrated with liquids with Mg-number between 0·58 and 0·61, close to the host basalt value (0·60), whereas the Group II samples equilibrated with more iron-rich melts with Mg-number ranging from 0·42 to 0·55. To define the geochemical affinity of the parental melt(s) of the NVL xenoliths we have also calculated the trace element compositions of the liquid(s) coexisting with the clinopyroxenes in the xenoliths, using partition coefficients between mineral and melt (D) taken from Skulski *et al.* (1994) and Halliday *et al.* (1995). This approach, however, involves some uncertainty in the derived liquid composition owing to the dependence of D on P and T.

The compositions of the calculated melts in equilibrium with the clinopyroxenes show similar profiles in a primitive mantle normalized trace element diagram (Fig. 10). Most of the calculated patterns fall within the field of the primitive Cenozoic basic lavas, especially those calculated for clinopyroxenes with the highest MgO and Cr_2O_3

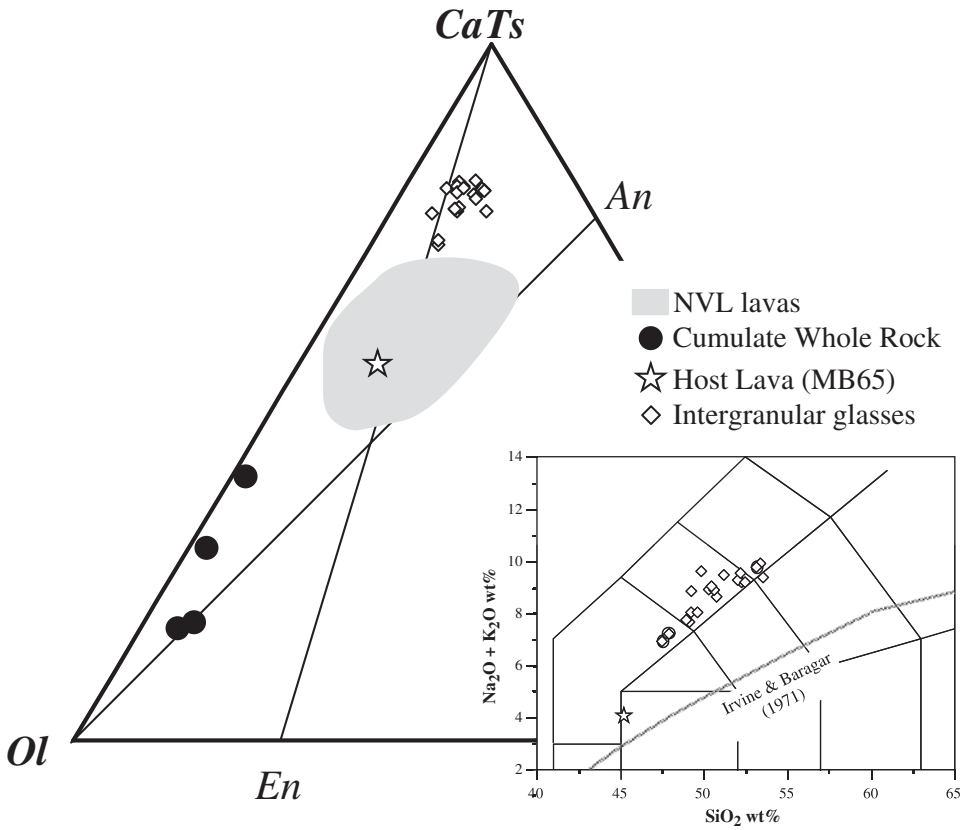

Fig. 5. Composition of interstitial glasses within the Browning Pass xenoliths plotted on a pseudo-ternary projection from Diopside (Di) in the basalt tetrahedron CaTs–Di–Ol–Q within the CMAS system (O'Hara, 1968): $C = (CaO - 3{\cdot}33P_2O5 + 2Na_2O + 2K_2O) \times 56{\cdot}08$; $M = (FeO + MnO + NiO + MgO - TiO_2) \times 40{\cdot}31$; $A = Al_2O_3 + Cr_2O_3 + Fe_2O_3 + Na_2O + K_2O + TiO_2) \times 101{\cdot}96$; $S = (SiO_2 - 2Na_2O - 2K_2O) \times 60{\cdot}09$ (all oxides in molar proportion). Data for NVL lavas are from Armienti *et al.* (1991). En, enstatite; An, plagioclase. In the inset the intergranular glasses are plotted on the total alkalis–silica classification diagram (Le Bas *et al.*, 1986). Discriminating curve between the alkaline and subalkaline fields is from Irvine & Baragar (1971).

contents (BRP3 and BRP19). These latter patterns are similar to that of the host lava (MB65). The calculated melt compositions of Cr-poor samples BRP 8 and BRP12 are close to those of a more Fe-rich alkaline basalt MDK (Mg-number = 0·51) and lava MB58 (Mg-number = 0·54), respectively, both of which belong to the Mt. Melbourne volcanic field (Armienti *et al.*, 1991; Table 10). A simple mass-balance calculation, based on major element compositions, rules out a genetic relationship between MB65 and MDK via a crystal fractionation process. However, assuming 11% fractionation of an olivine + clinopyroxene assemblage, sample MB58 can be obtained from sample MB65. The parental liquid calculated using the core of BR21d clinopyroxene is the most enriched in incompatible elements and appears significantly different from the others (Fig. 10); this can be ascribed to its more evolved character (Table 4) and to a diffusive metasomatic interaction that induced, in this sample, replacement of clinopyroxene by amphibole (Fig. 2b).

In summary, the composition of the melts calculated from the NVL cumulates and the Sr–Nd isotopic data indicates a genetic relationship with the primitive Cenozoic lavas and, in particular, with at least two different basic magma compositions similar to the MB65 host lava and MB58 and MDK alkali-basalts.

Thermobarometry

Thermobarometry (Table 11) of these cumulate rocks is difficult, as the mineral parageneses are not compatible with many established thermobarometers. However, the geobarometer developed by Nimis & Ulmer (1998) and Nimis (1999) can provide an estimate of the pressure of crystallization for xenolith clinopyroxene crystallizing directly from a magma; moreover, this does not require knowledge of the exact composition of the melt in equilibrium with the clinopyroxene. Using the temperature-independent calibration for anhydrous basic magmas, the calculated pressures range is between 0·6 and 0·9 GPa

Table 8: Trace element composition of clinopyroxenes

	BRP 3 core	BRP 3 rim	BRP 8 core	BRP 8 rim	BRP 8* rim	BRP 12 core	BRP 12* rim
V	206	223	293	350	467	202	378
Cr	7110	6370	3010	2605	2564	2400	725
Sc							
Sr	56·8	55	67·5	59·5	104	68·9	75·6
Y	10·2	11·2	17·3	23·6	30·1	19·65	22·7
Zr	27	28·5	52·3	80·5	102	57·35	79·6
La	1·79	1·76	3·37	3·62	4·31	3·44	3·92
Ce	6·83	7·05	11·50	14·70	17·50	12·96	14·60
Nd	6·83	7·10	11·10	15·60	19·20	12·35	14·50
Sm	2·45	2·55	3·48	4·92	6·38	4·11	5·03
Eu	0·76	0·83	1·08	1·84	2·32	1·43	1·74
Gd	2·60	2·46	3·66	5·73	7·29	4·12	5·43
Dy	2·12	2·15	3·30	4·72	6·10	3·72	4·55
Er	0·98	0·98	1·51	2·15	2·72	1·70	1·88
Yb	0·69	0·70	1·09	1·59	1·89	1·08	1·21

	BRP 19 core	BRP 19 rim	BRP 21 core	BRP 21 rim
V	210	214	419	393
Cr	5450	4970	680	1215
Sc			71	71
Sr	45·7	46·7	82·9	86·2
Y	10·9	11·7	26·9	26
Zr	22·2	27·5	132	120
La	2·02	1·93	8·63	8·11
Ce	6·72	6·49	28·7	26·3
Nd	5·96	6·01	22·9	21
Sm	1·90	1·93	6·49	6·31
Eu	0·69	0·71	2·11	2·16
Gd	2·13	2·65	6·89	6·78
Dy	2·01	2·44	5·76	5·23
Er	0·97	0·90	2·3	2·41
Yb	0·69	0·78	1·6	1·76

*Close to pyrometamorphic rim.

(Table 10). This range is compatible with the lack of garnet in all samples that constrains the equilibrium pressures to <1·4 GPa (Irving, 1974; Griffin *et al.*, 1984; Hirschmann & Stolper, 1996). Temperature estimations can be attempted using the Lindsley (1983) method, although the lack of coexisting orthopyroxene or pigeonite precludes the correct application of this geothermometer; its application to clinopyroxene not saturated in Ca implies that the estimated temperatures are minimum values. Bearing this in mind, the projection of clinopyroxene compositions onto Lindsley's isotherms for $P = 0{\cdot}5$–$1{\cdot}0$ GPa indicates temperatures of crystallization between 1100° and 1200°C (Table 10).

The textural and chemical characteristics of the pyroxenites and wehrlites and the lack of any evidence for spinel recrystallization from pre-existing garnet suggest that the clinopyroxenes last equilibrated at pressures similar to those at which they were segregated from their parental melts. In this respect the Putirka *et al.* (2003) clinopyroxene–liquid thermobarometer provides a way to estimate the P–T conditions for these lithologies not obtainable by other methods. This thermobarometer has been applied to reconstruct the crystallization history of basaltic systems and was calibrated for a wide range of bulk-rock compositions and pressures, encompassing both hydrous and dry conditions (Putirka & Condit, 2003; Putirka, 2008). Its original application was based on clinopyroxene–liquid pairs for which equilibrium was established on the basis of the Fe/Mg exchange coefficient $K_D^{cpx-lq}(Fe–Mg) = 0{\cdot}28$ ($K_D^{cpx-lq}(Fe–Mg) = [MgO^{liq}FeO^{cpx}]/[MgO^{cpx}FeO^{liq}]$, where MgO and FeO are molar fractions).

We observe that all the investigated cumulates contain olivine and pyroxene, and that experimental data indicate that both these minerals are early liquidus phases in the primitive basalts of the Cenozoic volcanic cycle (Orlando *et al.*, 2000). This allows us to apply Putirka's thermobarometer to the NVL cumulates, provided that for each pyroxene we can assess the composition of the coexisting equilibrium liquid. The Sr and Nd isotope data support a parental relationship between the cumulates and the Cenozoic basic lavas (Fig. 7). Starting from the trace element pattern of the parental melt reconstructed based on clinopyroxene/liquid partition coefficients (Fig. 10), the available population of near-primary melts can be compared with the calculated liquids; for each clinopyroxene composition we can select the natural melt whose trace element pattern is the most similar to the calculated one. In this method it is critical that the selected clinopyroxenes do not display pyrometamorphic textures and that their compositions obey the compositional criteria adopted by Putirka *et al.* (2003).

The major element composition of the inferred natural melt is then checked for equilibrium with clinopyroxene, following the thermobarometer requirements. In particular, if we consider that only olivine and clinopyroxene are the liquidus phases (Armienti *et al.*, 1991), the composition of this melt may differ from that at the initiation of cumulate formation only by the cotectic subtraction or addition of these two phases; equilibrium can be restored by subtracting or adding olivine + clinopyroxene to the whole-rock composition (Armienti *et al.*, 2010).

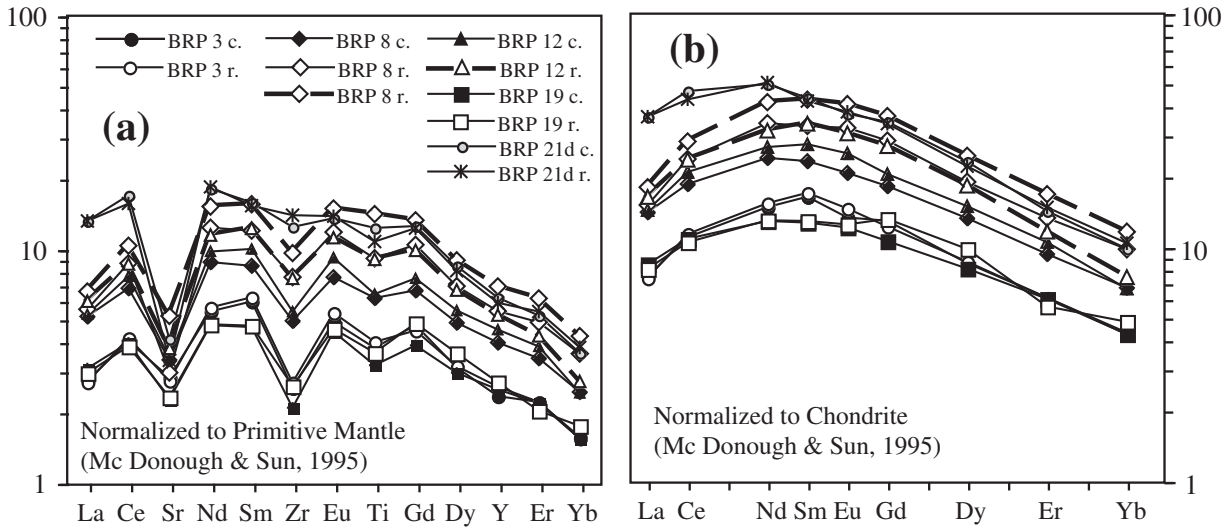

Fig. 6. (a) Primitive mantle-normalized trace element patterns and (b) chondrite-normalized REE patterns for clinopyroxenes in the NVL pyroxenites and wehrlites. Normalizing values from McDonough & Sun (1995). c., core; r., rim.

Table 9: Sr, Nd and oxygen isotope composition of minerals separated from cumulates

	Clinopyroxene						Olivine			
	$^{87}Sr/^{86}Sr$	2σ	$^{143}Nd/^{144}Nd$	2σ	$\varepsilon Nd(t=0)_{cpx}$	$\delta^{18}O$ (‰)	σ	$\delta^{18}O$ ‰	σ	$\Delta^{18}O_{cpx-ol}$
BPR1						5·48	0·11	5·24	0·08	0·24
BPR3	0·702943	0·000007	0·512950	0·000009	6·1	5·29	0·05	5·72	0·15	−0·43
BPR7						5·16	0·05			
BPR8	0·702921	0·000007	0·512949	0·000007	6·1	5·53	0·12	5·17	0·16	0·36
BPR12	0·702930	0·000008	0·512949	0·000005	6·1	5·24	0·04	5·16	0·01	0·09
BPR19	0·702955	0·000006	0·512954	0·000007	6·2	5·20	0·15	5·36	0·07	−0·16
BPR20						5·20	0·07	5·41	0·13	−0·21
BPR21	0·702892	0·000006	0·512937	0·000005	5·8	5·17	0·02	5·00	0·02	0·17

Calculations are performed using a code that adds an infinitesimal amount of MgO to the system and then readjusts the liquid composition on the basis of olivine and pyroxene stoichiometry and mass ratio, to allot suitable amounts of the remaining elements. The relative amounts of olivine and clinopyroxene are established by the ratio of these phases observed in the cumulate rocks. The continuous readjustment of the liquid composition by the addition of equilibrium olivine and clinopyroxene is stopped when the computed liquid is in equilibrium with the given pyroxene analysis, satisfying the condition $K_D^{cpx-liq} = 0 \cdot 28$ (Armienti *et al.*, 2010). Mineral subtraction or addition within 5% was considered as appropriate to consider the selected melt suitable for T and P estimates by Putirka's geothermobarometer. In fact, because we infer the liquid in equilibrium with a given clinopyroxene by its trace element composition, a higher amount of subtraction or addition would induce bias on the trace element composition of the reconstructed equilibrium melt, in contrast to the approach used to identify the liquid from which a given clinopyroxene crystallized.

In the context of this study melt compositions similar to those of MB65 host lava, and MB58 and MDK basalts may be considered the parental liquids of all the studied xenoliths, with the exception of BPR2ld, owing to the noticeable metasomatic modification of this sample. Table 11 reports the thermobarometric estimates obtained by the above method; these are slightly higher than those obtained by the Nimis & Ulmer (1998) approach.

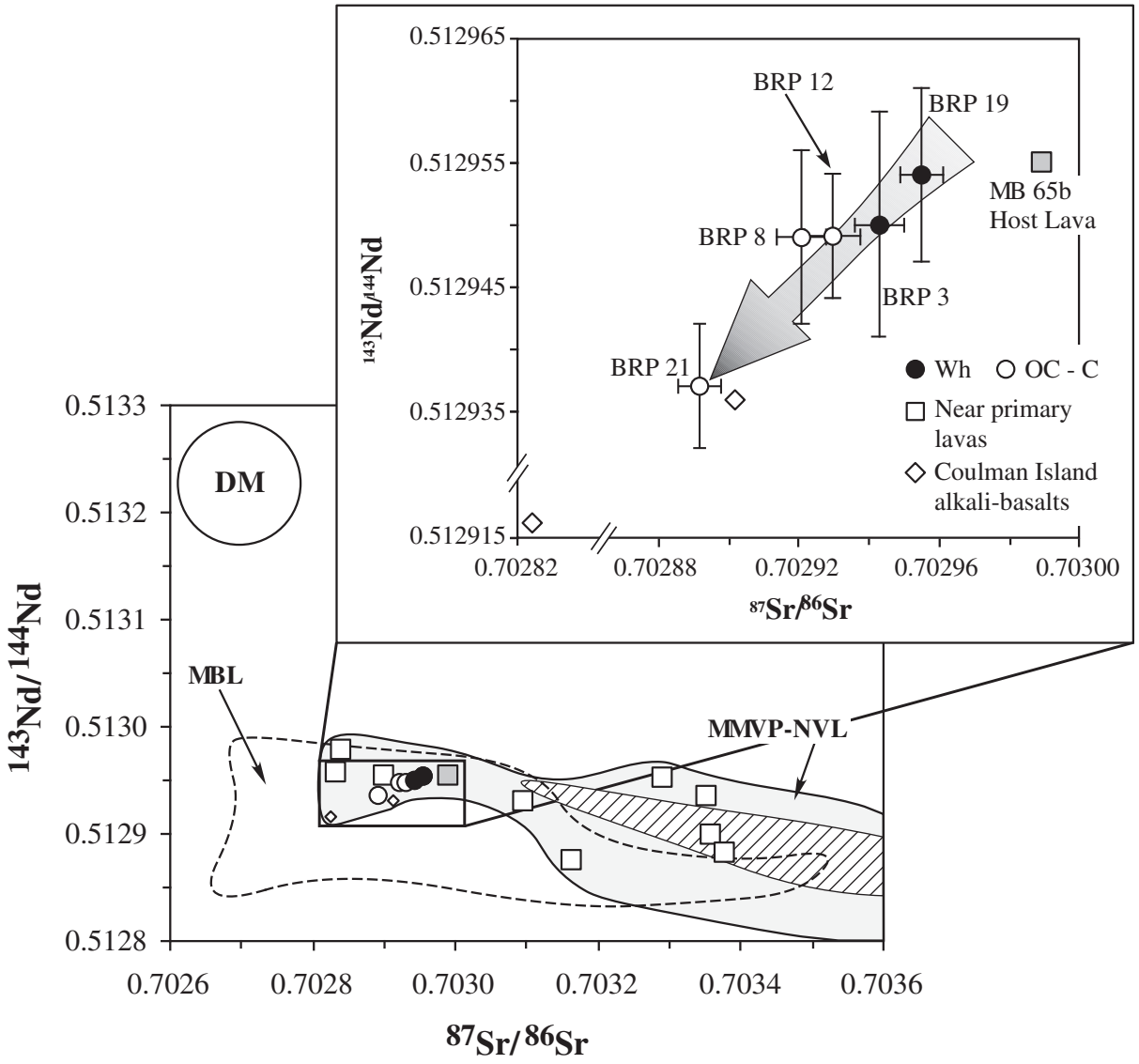

Fig. 7. Sr–Nd isotopic compositions of clinopyroxene mineral separates from the Browning Pass xenoliths, $^{87}Sr/^{86}Sr$ and $^{143}Nd/^{144}Nd$ ratios for Cenozoic near-primary lavas (Nardini *et al et al.*, 2009) and two Cenozoic alkaline-basalts from Coulman Island (Rocholl *et al.*, 1995). The diagonal-shaded field encompasses data for plutons and dyke swarms emplaced during the onset of Cenozoic magmatic activity (Rocchi *et al.*, 2002); DM is the depleted mantle end-member of Zindler & Hart (1986); the MMVP-NVL and MBL fields include volcanic rocks from the McMurdo Volcanic Province–northern Victoria Land and Marie Byrd Land respectively (data are from GEOROC: http//georoc.mpch-mainz.gwdg.de/georoc/). Wh, OC and C abbreviations refer to wehrlite, olivine-clinopyroxenite and clinopyroxenite respectively. The arrow indicates the decrease in Sr–Nd isotope composition of the clinopyroxenes owing to metasomatism.

Further constraints on the P–T conditions at which the cumulates formed have been obtained based on the analysis of CO_2-bearing fluid inclusions trapped in clinopyroxene and olivine crystals. These data indicate temperatures of about 1200°C and minimum 'trapping' pressures of ~0·8 GPa (P. Armienti, unpublished data), which fall on the same trend as defined by the data based on the Putirka thermobarometer.

Comparison of estimated cumulate parental liquid T and P with thermodynamic models

To better constrain the P–T conditions of formation of the cumulates, we have modeled the evolution of the estimated parental melts using the pMELTS algorithm (Ghiorso *et al.*, 2002), assuming equilibrium crystallization from melts with the composition of MB65 and MDK at

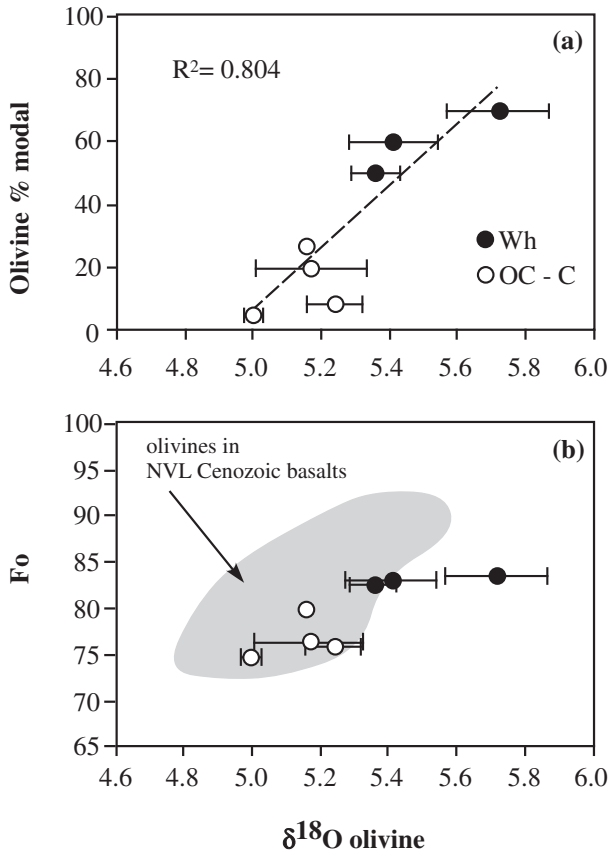

Fig. 8. Oxygen isotope composition of olivines ($\delta^{18}O$ olivine VSMOW‰) vs (a) modal proportion and (b) Fo content (mol %). Horizontal error bars represent the 2σ of $\delta^{18}O$ values measured for each sample and are centered on average compositions.

0·9 GPa (the average value of the range of estimated P). Oxygen fugacity conditions (fO_2) were fixed at 1 log unit above the fayalite–magnetite–quartz buffer (FMQ) as suggested by the fO_2 estimate using the Ballhaus *et al.* (1991) formulation applied to an olivine–spinel pair in BRP19. At anhydrous conditions, the calculated phase relations (cpx → cpx + ol) and crystallization temperature ($T > 1250°C$) for both MB65 and MDK are in contrast to the observed petrography of the cumulates, which suggests an ol → ol + cpx crystallization sequence and temperatures $T < 1200°C$ (Table 11).

The widespread occurrence of amphibole in the McMurdo volcanic products as phenocrysts, megacrysts and cumulate-forming phases (Gamble & Kyle, 1987; Gamble *et al.*, 1988; Beccaluva *et al.*, 1991; Hornig *et al.*, 1991) implies the presence of significant amounts of water in the NVL basic melts. An estimation of the initial water content of the host lava MB65 can be made taking into account the similar incompatible behaviour of H_2O and Ce and Nd (Zajacz *et al.*, 2007, and reference therein); using an $H_2O/(Ce + Nd)$ ratio equal to 95 ± 30 (Michael, 1988) and an H_2O/Ce ratio equal to 210 ± 20 (Simons *et al.*, 2002) the estimated water content of MB65 is between 0·9 and 1·6 wt % and between 1·3 and 1·8 wt %, respectively. Thus for pMELTS calculations we assumed as initial water contents the average values of 1·4, 1·6 and 1 wt % for basalts MB65, MB58 and MDK, respectively.

Results provided by pMELTS are generally in good agreement with the textural and mineralogical observations and P–T estimates, despite some differences in the predicted clinopyroxene chemistry that may be due to the assumed starting conditions, the assumption of perfect equilibrium crystallization in a closed system and uncertainties in the thermodynamic model. In particular, according to the model for equilibrium crystallization of MB65 at T between 1195 and 1180°C the resultant olivine/clinopyroxene ratios (2·6–1·2) are comparable with those of the wehrlites (2·8–1·0). The forsterite range of the modeled olivines is also similar to that of olivine in the cumulates (83·3–81·9 and 83·6–82·6, respectively), whereas the Mg-number values of the model clinopyroxenes and of the residual melts (0·77–0·75 and 57–55, respectively) are lower than those of the cumulate clinopyroxenes and the calculated equilibrium liquids (83–81 and 61–58, respectively). Olivine-clinopyroxenites and clinopyroxenites BRP1, BRP7 and BRP8 (ol/cpx = 0·03–0·28) are well matched starting from an MDK composition over a temperature interval of 1120–1170°C (ol/cpx = 0·02–0·23), close to that estimated using the integrated Putirka *et al.* (2003) method. For basalt sample MDK, the model clinopyroxenes show differences in composition with respect to the cpx in the cumulates, with lower Mg-number (0·69–0·72 and 0·73–0·80, respectively), whereas model and natural olivine have the same Fo range (~76 for BRP1 and BRP8, ~73 for BRP7). Olivine-clinopyroxenite BRP12 matches the solid assemblage obtained using basalt MB58 for 1175–1180°C, but can be also modeled starting from basalt MB65 after 14% of crystallization at 1165°C.

Origin of oxygen isotope heterogeneity

The oxygen isotope compositions of olivine and clinopyroxene from the NVL cumulates reveal different extents of inter-mineral disequilibrium that can be explained as the consequence of $\delta^{18}O$ partial resetting by metasomatic reaction with melts or fluids. According to the expected oxygen isotope fractionation at mantle conditions, pyroxenes should be richer in ^{18}O by ~0·4‰ than coexisting olivines; in contrast, most of samples have high olivine $\delta^{18}O$ values coupled with relatively low $\delta^{18}O$ values of coexisting clinopyroxenes (Table 9). The cpx–ol disequilibrium is particularly evident for the wehrlite samples, which show the highest deviation from the expected equilibrium value at mantle conditions. Because oxygen diffusion in clinopyroxene is 1–2 orders of magnitude faster than olivine (Farver, 1989; Rosenbaum *et al.*, 1994), clinopyroxene in oxygen isotope compositions may be

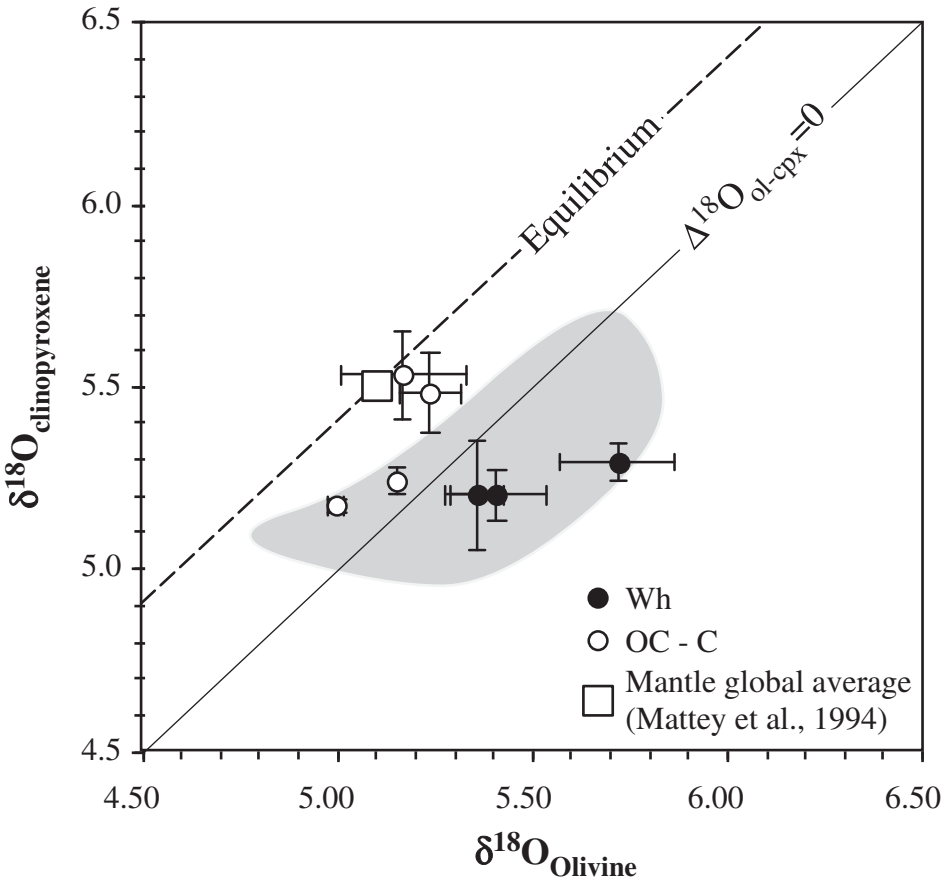

Fig. 9. Oxygen isotope composition of olivine and clinopyroxene mineral separates. Dashed line represents the equilibrium $\Delta^{18}O_{ol-cpx}$ for spinel peridotite xenoliths worldwide (Mattey *et al.*, 1994). The grey shaded field indicates NVL spinel peridotites from Perinelli *et al.* (2006).

preferentially reset. This implies that the small variability in $\delta^{18}O$ of the xenolith clinopyroxenes may represent the attainment of isotope equilibrium of this phase with a metasomatic melt(s) or fluid(s). The metasomatic agent was ^{18}O-depleted ($\delta^{18}O = 5{\cdot}4$–$5{\cdot}5‰$ or less, where $\Delta^{18}O_{melt-cpx} = 0{\cdot}2$ at $T > 1000°C$; Zhao & Zheng, 2003) with respect to the cumulate O isotope composition ($\delta^{18}O$ in the range 5·8–6·3‰, where $\Delta^{18}O_{melt-ol} = 0{\cdot}6$; Zhao & Zheng, 2003). Additionally, the $\delta^{18}O$ of olivine, owing to its slow re-equilibration time, may provide the best constraint for the initial $\delta^{18}O$ of the cumulates. At mantle temperatures, oxygen diffusion in clinopyroxene is of the order of $10^{-15}\,cm^2\,s^{-1}$ (Rosenbaum *et al.*, 1994; Deines & Haggerty, 2000). A rough estimation of the time required for isotope equilibration of a crystal 4 mm in size (the size of the larger crystals in analyzed samples) should be about 5 Myr. This suggests that the metasomatic event responsible for the modification of the O isotope composition and, probably, of the observed enrichments in incompatible elements in clinopyroxene rims, is closely linked to the Cenozoic magmatism. The differences observed between the wehrlites and pyroxenites and the inter-mineral disequilibria indicate that the parental melts of the cumulates and the metasomatic agents originated from a mantle source heterogeneous in its ^{18}O composition, as also pointed out by Nardini *et al.* (2009).

Evolution of the parental melt and geodynamic relationships

Barometric estimates and the compositional features of the NVL cumulate xenoliths suggest an origin linked to the rising path of different batches of Cenozoic primary melts that stall and crystallize close to the present position of the Moho in this region (20–25 km; McGinnis *et al.*, 1985; Fitzgerald *et al.*, 1987; Trehu *et al.*, 1989), where the crust–mantle density contrast influences the ascent rate of mantle melts. The temperatures of crystallization of the cumulates provided by our adaptation of Putirka's themobarometer (1130–1190°C), are considerably different from those of the primitive NVL basaltic melts rising adiabatically from a mantle source with a potential temperature of 1250–1310°C (Orlando *et al.*, 1997), and from the temperature of the Moho derived by peridotite thermobarometry (950–1050°C) and from heat fluxes (Armienti & Perinelli,

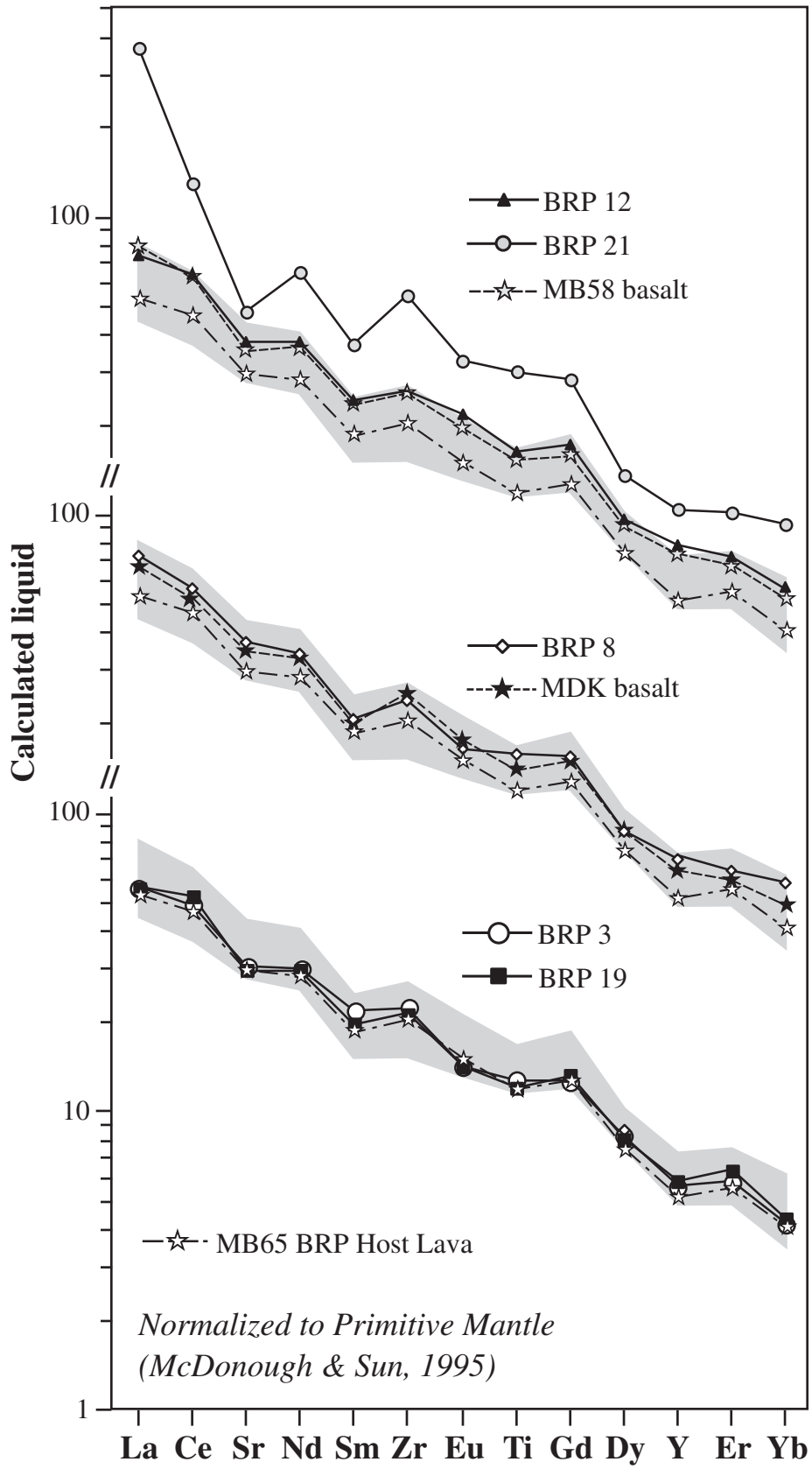

Fig. 10. Primitive mantle normalized trace element compositions of calculated liquids at equilibrium with clinopyroxenes from the Browning Pass pyroxenites and wehrlites. Compositions were calculated using the clinopyroxene/liquid partition coefficients of Skulski *et al.* (1994) and Halliday *et al.* (1995) using only the core composition of the clinopyroxenes. MB58 and MDK are alkali basalts from Armienti *et al.* (1991). The field for primitive Cenozoic lavas (Nardini *et al.*, 2009) is also shown (grey shaded).

Table 10: Major and trace element composition of basalts inferred to be similar to cumulate parental melts (data from Armienti et al.*, 1991)*

	MB58	MDK
SiO_2	44·65	45·82
TiO_2	2·95	2·89
Al_2O_3	16·38	16·63
FeO_t	12·08	11·80
MnO	0·21	0·20
MgO	7·83	6·72
CaO	8·94	9·27
Na_2O	3·73	3·45
K_2O	1·33	1·39
P_2O_5	0·68	0·69
LOI	0·70	0·76
Mg-no.	0·54	0·50
V	178	198
Cr	112	218
Co	33	35
Ni	57	113
Rb	43	42
Sr	841	717
Y	28	27
Zr	269	280
Nb	79	75
Ba	348	362
La	54·2	51·1
Ce	110	106
Nd	50·1	45·9
Sm	10·2	9·4
Eu	3·2	3·0
Gd	9·0	8·5
Dy	6·5	6·1
Er	3·0	2·9
Yb	2·3	2·2
Lu	0·3	0·3

2010). The studied cumulates were probably formed along the conduit walls of rising magma batches and may represent the contact between the cooler mantle and rising magma. According to heat conduction theory (e.g. Turcotte & Schubert, 2002) at a distance d from the contact, the temperature T is provided by the equation

$$(T - T_a)/(T_m - T_a) = 1/(1 + \mathrm{erf}\ \lambda) \qquad (1)$$

where T_a and T_m are the ambient mantle and magma temperatures, respectively, $\lambda = -d/(2\sqrt{kt})$, k is the thermal conductivity and t is time.

Table 11: Temperature and pressure estimates for Browning Pass xenoliths

	T (°C) (Lindsley, 1983)	T (°C) (Putirka *et al.*, 2003)	P (GPa) (Putirka *et al.*, 2003)	P (GPa) (Nimis & Ulmer, 1998)
BRP1	1160	1137	0·84	0·83
BRP 3	1160	1173	0·82	0·55
BRP7	1130	1126	0·80	0·67
BRP 8	1170	1151	0·88	0·84
BRP 12	1180	1169	0·95	0·69
BRP 19	1200	1186	1·06	0·55
BRP 20	1150	1164	0·98	0·61
BRP 21	1130			0·69
BRP 22	1120			0·58

The error associated with Nimis & Ulmer (1998) barometer is ±0·2 GPa whereas the uncertainties associated with thermometer and barometer calibration of Putirka *et al.* (2003) model are ±33 K and ±0·2 GPa, respectively.

The temperature (T_c) at the conduit walls ($d = 0$) is half the sum of the ambient and magma temperatures:

$$T_c = 0 \cdot 5(T_m + T_a). \qquad (2)$$

The distance of the cumulate from the wall-conduit contact is unknown, thus this approach may provide temperatures higher than the actual T_c. The values of T_c determined from the cumulates bracket the maximum temperature values that could be attained in the conduit walls at a given depth (Fig. 11). Equation (2) can be solved at various depths to estimate the actual value of T_a; that is, the likely temperature of the mantle at the time of crystallization of the cumulates (Fig. 11, squares). The resulting temperature estimates provide an independent assessment of Moho temperature that is very similar to the value obtained by Armienti & Perinelli (2010) on the basis of spinel-peridotite thermobarometry and surface heat fluxes.

The genesis of the NVL mantle cumulates may be interpreted as the effect of local mantle heating related to the switch of geothermal gradient from values typical of dynamic rifting (~0·5°C km^{-1}) to much higher values (3°C km^{-1}). This switch is mostly responsible for the amount and timing of the Cenozoic uplift of the Transantarctic Mountains (Armienti & Perinelli, 2010). Many lines of evidence have led to suggestions that the development of the Ross Sea Rift system and associated magmatic activity in northern Victoria Land is linked to dextral transtensional movements connected with an important reorganization in plate kinematics in the Southern Hemisphere, rather than to the action of a thermally active mantle plume (Rocchi *et al.*, 2002, 2003, 2005; Storti *et al.*, 2007). The geochemical and isotopic

compositions of the Cenozoic basalts reported by Nardini *et al.* (2009) support a model in which the source of the primary basalts is in the sublithospheric mantle, metasomatized during an earlier extensional event that affected the WARS in the Late Cretaceous. After this first phase of Ross Sea opening, at the boundary between the thick East Antarctic craton and the thinned crust of the Ross Sea, an 'edge effect' in the mantle circulation pattern (Faccenna *et al.*, 2008) may have provided the heat source to warm the lithospheric mantle beneath northern Victoria Land (Armienti & Perinelli, 2010). The formation of the wehrlites and pyroxenites necessarily follows the change of the mantle thermal gradient induced by the 'edge effect', probably during the Late Cenozoic.

Isotopic data help to further constrain the Cenozoic events that led to the development of the Mt. Melbourne Volcanic Province. Rocchi *et al.* (2002, 2005) and Storti *et al.* (2007) suggested that during Eocene–Oligocene times the reactivation of Palaeozoic lithospheric discontinuities in northern Victoria Land was due to an increase in the differential velocity across the Southern Ocean fracture zones. This induced local mantle decompression and partial melting, providing the magmas that were initially emplaced as plutons and dyke swarms (Rocchi *et al.*, 2002). From the Late Miocene to the present, the craton-ward mantle flow led to collapse of the rift shoulders and normal faulting,which favored the rise of magmas to the surface (Nardini *et al.*, 2009). Even if the cumulates represent the crystallization products of the earliest rising melts, the lack of annealing textures in these rocks appears to exclude an Eocene–Oligocene age. Because their Sr–Nd isotope compositions are largely depleted compared with the composition of the Eocene–Oligocene intrusive rocks, and more closely approach those of the Late Miocene volcanic rocks (Fig. 7), we favor a Late Miocene origin for the wehrlites and pyroxenites, arguing that their formation follows the change of the mantle geotherm induced by the edge effect. Indeed, at the onset of the Cenozoic magmatism the thermal profile of the lithosphere would have not allowed the formation of cumulates at the estimated temperatures.

Figure 7 shows that the near-primary melts and their cumulates reflect an enriched source (relative to the depleted mantle, DM), and that the trend of the wehrlites and pyroxenites cannot be related to any crustal contamination effect. Indeed, the NVL cumulates exhibit cryptic and modal evidence of metasomatism, which we ascribe to migrating mantle fluids or melts. The oxygen isotope data also rule out any contamination by crustal rocks (Figs 8 and 9), supporting the contention that the source of the metasomatic agent is in the upper mantle. Compared with the cumulate parental melts, the clinopyroxenes of the modally metasomatized cumulate BRP2l indicate that the metasomatizing agent has a lower $^{87}Sr/^{86}Sr$ and $^{143}Nd/^{144}Nd$ ratio and also lower $\delta^{18}O$. The Sr–Nd isotope and $\delta^{18}O$ composition (5·13–5·76‰; Nardini *et al.*, 2009) of alkali basalts from Coulman Island, a shield volcano north of the MMVP, plot close to BRP2l on the Sr–Nd cumulate trend (Fig. 7). This suggests that a mantle melt with a radiogenic and stable isotope composition similar to that of the Coulman Island basalts, which never erupted in the NVL area, could have been the metasomatizing agent of the NVL cumulates. Moreover, based on diffusion data for oxygen isotopes and the occurrence and the extent of inter-mineral disequilibrium, combined with the incompatible element zoning in some clinopyroxenes, the timing of the metasomatic event is constrained to be within the period of the Cenozoic magmatism. Temporal relationships between magmatism linked to lithospheric rifting and mantle metasomatism have been documented in a variety of provinces worldwide, suggesting that metasomatic processes occur before mantle xenoliths are entrapped in the host magma (e.g. Francis, 1976; Menzies *et al.*, 1985; Perkins *et al.*, 2006).

The isotopic characteristics of the metasomatizing agent are consistent with a melting of HIMU-type mantle source enriched in ^{238}U but characterized by low $\delta^{18}O$. Commonly such sources have been linked to ancient subducted oceanic lithosphere (Hofmann, 1997). However, even if in the geological record of northern Victoria Land there is evidence for episodes of subduction related to Paleozoic orogenic events, there is no need to invoke such a source, as partial melts formed at the expense of the lithospheric mantle itself by 'short-term metasomatic' processes can reproduce the key major, trace element and isotopic features of within-plate alkaline magmas (Pilet *et al.*, 2004, 2008). The short-term metasomatic model envisages a vein-plus-wall process in which melts, produced during an early phase of decompression mantle melting, form veins in the overlying lithospheric mantle by a percolative fractional crystallization process. The high degree of partial melting of such low-solidus temperature veins induced by progressive mantle decompression and/or the onset of a local thermal perturbation better account for the major and trace element compositions of alkali basalts than low-degree partial melting (<1%) of subducted oceanic crust (Pilet *et al.*, 2008). This model can account for the Sr–Nd–Pb isotopic compositions of NVL near-primary melts (Nardini *et al.*, 2009) and could also explain the observed variation in their ^{18}O composition. The occurrence of extensive ^{18}O isotope heterogeneity in the NVL lithospheric mantle has also been revealed in peridotite xenoliths from two localities close to the Browning Pass (NVL) area (Perinelli *et al.*, 2006). Both suites include xenoliths modally or cryptically modified by a metasomatic event linked to the Cenozoic magmatism, and unmetasomatized peridotites. The ^{18}O composition of the latter

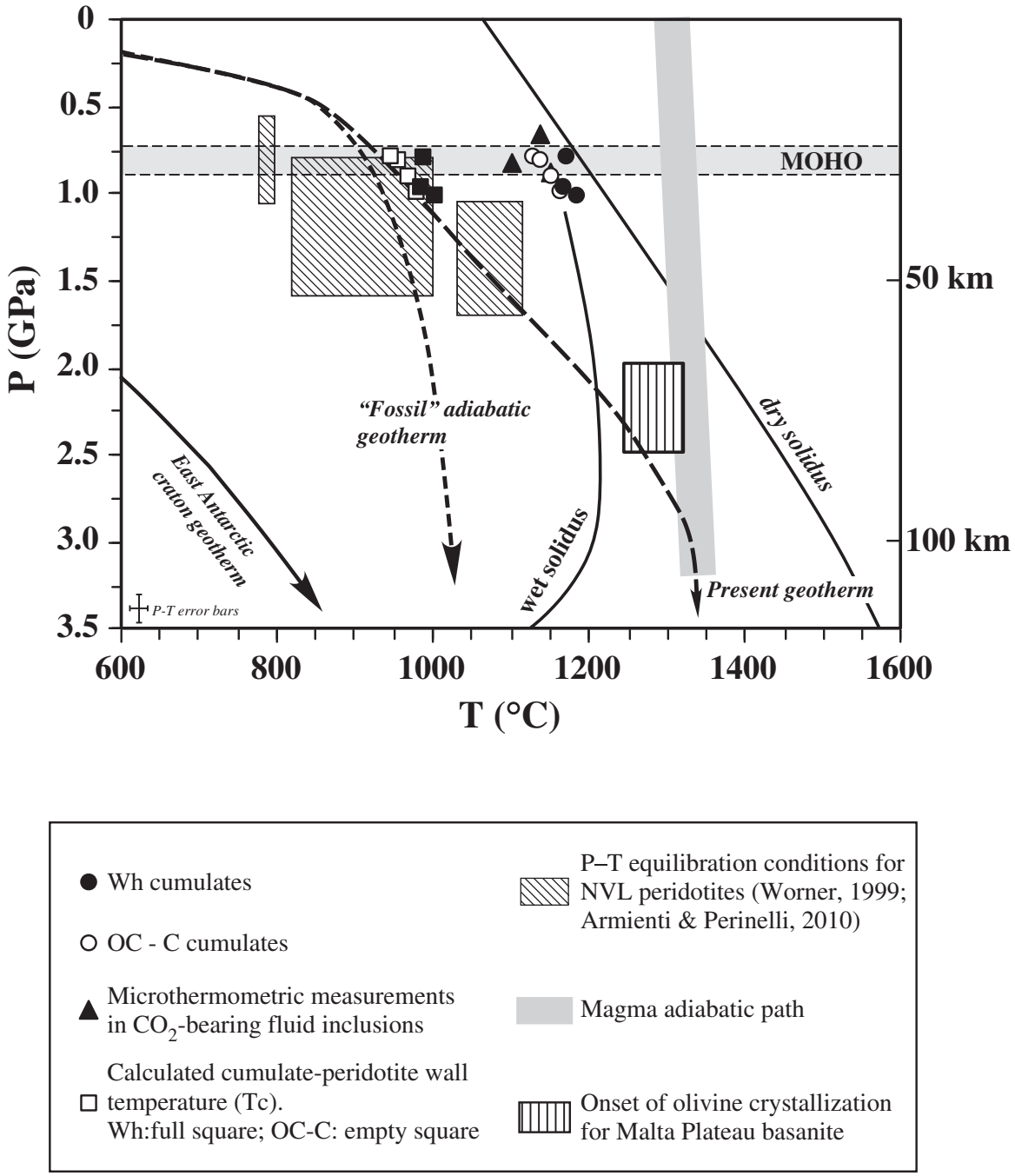

Fig. 11. Pressure and temperature estimates for the NVL pyroxenite and wehrlite xenoliths. Water-saturated (wet) and dry peridotite solidi are after Green & Falloon (1998). The Moho depth is after Trehu *et al.* (1989). *P–T* data for NVL spinel-peridotite xenoliths are from Wörner (1999) and Armienti & Perinelli (2010). The error bars refer to the size of the uncertainties in Putirka's thermobarometry method (Putirka *et al.*, 2003). 'Fossil' adiabatic and present-day geotherms suggest a rise in the geothermal gradient in northern Victoria Land (from 0·5 to ~3°C km^{-1}) during the evolution of the rift system (Armienti & Perinelli, 2010).

($\delta^{18}O = 5{\cdot}12–5{\cdot}62‰$ for clinopyroxenes from unmetasomatized peridotite xenoliths) could represent the local upper mantle before the Cenozoic rifting, implying ancient $\delta^{18}O$ heterogeneities in the NVL mantle.

We can explain with a simple mechanism of *in situ* evolution the isotopic heterogeneity of the parental and metasomatizing melts, as revealed by the geochemistry of the Browning Pass cumulates. Geochemical variability simply

reflects variable contributions to the production of the Cenozoic magmas by two end-members represented by (1) the metasomatic veins or domains emplaced during the Late Cretaceous amagmatic phase of Ross Sea rifting and (2) the surrounding depleted lithospheric mantle (Nardini *et al.*, 2009), in a geodynamic scenario of a perturbed local thermal regime following the development of edge-driven convection of asthenospheric mantle at the boundary between the thick East Antarctic craton and thin Ross Sea lithosphere.

CONCLUSIONS

Pyroxenite and wehrlite xenoliths hosted in alkali basalts in northern Victoria Land can be considered as early fractionates of near-primary mantle melts feeding Cenozoic volcanic activity, at relatively shallow mantle depths (approximately Moho depth). Thermobarometric data, along with compositional and regional tectonic relationships, suggest that cumulates may have formed in the Late Miocene, following warming of the lithospheric mantle owing to a local enhancement of asthenospheric circulation induced by an 'edge-driven effect', soon after the opening phase of the Ross Sea. After their formation, the cumulates were affected by different degrees of metasomatism that produced amphibole as a replacement of clinopyroxene (modal metasomatism) and modified the trace element and Sr–Nd–O-isotope composition (cryptic metasomatism). Isotopic modifications, resulting in a decrease in the $^{87}Sr/^{86}Sr$ and $^{143}Nd/^{144}Nd$ ratios, and also of $\delta^{18}O$ in the more evolved cumulates, suggest that an alkali basaltic melt(s), similar to that sampled in the area of Coulman Island, may be identified as the possible metasomatic agent(s). This supports the observation that in the Mt. Melbourne region some of the resultant mantle melts did not reach the surface, and also that the differences in isotopic composition between the parental magmas and the melt(s) that metasomatized the ultramafic cumulates reflect the contribution of two different sources to the Antarctic Cenozoic magmatism. These sources may be represented by early metasomatic veins or domains emplaced during an amagmatic phase at the beginning of Ross Sea opening, and by a depleted lithospheric mantle domain. Magma generation processes are controlled by the variation of the local thermal regime imposed by variations in the flow of the underlying asthenosphere induced by a lithospheric step at the boundary between the East Antarctic cratonic block and the thinner lithosphere beneath the Ross Sea.

ACKNOWLEDGEMENTS

We are very grateful to M. A. Menzies, K. S. Panter and an anonymous referee for their constructive reviews, which helped improve the quality of the paper.

FUNDING

This work was supported by PNRA project, grants PEA2004/2006.

REFERENCES

Adam, J. & Green, T. H. (1994). The effects of pressure and temperature on the partitioning of Ti, Sr and REE between amphibole, clinopyroxene and basanitic melts. *Chemical Geology* **117**, 219–233.

Akinin, V. V., Sobolev, A. V., Ntaflos, T. & Richter, W. (2005). Clinopyroxene megacrysts from Enmelen melanephelinitic volcanoes (Chukchi Peninsula, Russia): application to composition and evolution of mantle melts. *Contributions to Mineralogy and Petrology* **150**, 85–101.

Armienti, P. & Baroni, C. (1999). Cenozoic climatic change in Antarctica recorded by volcanic activity and landscape evolution. *Geology* **27**, 617–620.

Armienti, P. & Perinelli, C. (2010). Cenozoic thermal evolution of lithospheric mantle in northern Victoria Land (Antarctica): evidences from mantle xenoliths. *Tectonophysics* **486**, 28–35.

Armienti, P., Civetta, L., Innocenti, F., Manetti, P., Tripodo, A., Villani, L. & Vita, G. (1991). New petrological and geochemical data on Mt. Melbourne volcanic field, northern Victoria Land, Antarctica. (II Italian Antarctic expedition). *Memorie della Società Geologica Italiana* **46**, 397–424.

Armienti, P., Gasperini, D., Perinelli, C. & Putirka, K. D. (2010). A new model for estimating deep-level magma ascent rates from thermobarometry: an example from Mt. Etna and implications for deep-seated magma dehydration. *Acta Vulcanologica, Special Issue dedicated to Professor Fabrizio Innocenti* 145–158.

Asprey, L. B. (1976). The preparation of very pure F_2 gas. *Journal of Fluorine Chemistry* **7**, 359–361.

Baker, J. A., Macpherson, C. G., Menzies, M. A., Thirlwall, M. F., Al-Kadisi, M. & Mattey, D. P. (2000). Resolving crustal and mantle contributions to continental flood volcanism, Yemen: constraints from mineral oxygen isotope data. *Journal of Petrology* **41**, 1805–1820.

Ballhaus, C., Berry, R. F. & Green, D. H. (1991). High pressure experimental calibration of the olivine–orthopyroxene–spinel oxygen geobarometer: implications for the oxidation state of the upper mantle. *Contributions to Mineralogy and Petrology* **107**, 27–40.

Barnes, S. J. & Roeder, P. L. (2001). The range of spinel compositions in terrestrial mafic and ultramafic rocks. *Journal of Petrology* **42**, 2279–2302.

Beccaluva, L., Coltorti, M., Orsi, G., Saccani, E. & Siena, F. (1991). Nature and evolution of subcontinental lithospheric mantle of Antarctica: evidence from ultramafic xenoliths of the Melbourne volcanic province (northern Victoria Land, Antarctica). *Memorie della Società Geologica Italiana* **46**, 353–370.

Behrendt, J. C., LeMausurier, W., Cooper, A. K., Tessensohn, F., Tréhu, A. & Damaske, D. (1991). Geophysical studies of the West Antarctic Rift System. *Tectonics* **10**, 1257–1273.

Behrendt, J. C., LeMausurier, W. & Cooper, A. K. (1992). The West Antarctic Rift System—a propagating rift captured by a mantle plume? In: Yoshida, Y., Kaminuma, K. & Shiraishi, K. (eds) *Recent Progress in Antarctic Earth Science. Proceedings of the Sixth International Symposium on Antarctic Earth Sciences*, Terra Sci., Tokyo, Japan, pp. 315–322.

Bodinier, J. L., Fabries, J., Lorand, J. P., Dostal, J. & Dupuy, C. (1987*a*). Geochemistry of amphibole pyroxenite veins from the

Lherz and Freychinede ultramafic bodies (Aeriege, French Pyrenees). *Bulletin de Minéralogie* **110**, 345–358.

Bodinier, J. L., Guiraud, M., Fabries, J., Dostal, J. & Dupuy, C. (1987*b*). Petrogenesis of layered pyroxenites from the Lherz, Freychinede and Prades ultramafic bodies (Ariege, French Pyrenees). *Geochimica et Cosmochimica Acta* **51**, 279–290.

Chand, S., Radhakrishna, M. & Subrahmanyam, C. (2001). India–East Antarctica conjugate margins: rift-shear tectonic setting inferred from gravity and bathymetry data. *Earth Planetary Science Letters* **185**, 225–236.

Chazot, G., Lowry, D., Menzies, M. & Mattey, D. (1997). Oxygen isotopic composition of hydrous and anhydrous mantle peridotites. *Geochimica et Cosmochimica Acta* **61**, 161–169.

Chiba, H., Chacko, T., Clayton, R. N. & Goldsmith, J. R. (1989). Oxygen isotope fractionations involving diopside, forsterite, magnetite, and calcite: applications to geothermometry. *Geochimica et Cosmochimica Acta* **53**, 2985–2995.

Coltorti, M., Beccaluva, L., Bonadiman, C., Faccini, B., Ntaflos, T. & Siena, F. (2004). Amphibole genesis via metasomatic reaction with clinopyroxene in mantle xenoliths from Victoria Land, Antarctica. *Lithos* **75**, 115–139.

Deines, P. & Haggerty, S. E. (2000). Small-scale oxygen isotope variations and petrochemistry of ultradeep (>300 km) and transition zone xenoliths. *Geochimica et Cosmochimica Acta* **64**, 117–131.

Dobosi, G., Downes, H. & Mattey, D. (1998). Oxygen isotope ratios of phenocrysts from alkali basalts of the Pannonian basin: Evidence for an O-isotopically homogeneous upper mantle beneath a subduction-influenced area. *Lithos* **42**, 213–223.

Faccenna, C., Rossetti, F., Becker, T. W. & Danesi, S. (2008). Recent extension driven by mantle upwelling beneath the Admiralty Mountains (East Antarctica). *Tectonics* **27**, TC4015, doi:10.1029/2007TC002197.

Farver, J. R. (1989). Oxygen self-diffusion in diopside with application to cooling rate determinations. *Earth and Planetary Science Letters* **92**, 386–396.

Fitzgerald, P. G. (1994). Thermochronologic constraints on post-Paleozoic tectonic evolution of the central Transantarctic Mountains. Antarctica. *Tectonics* **132**, 818–836.

Fitzgerald, P. G. & Stump, E. (1997). Cretaceous and Cenozoic episodic denudation of the Transantarctic Mountains, Antarctica: new constraints from apatite fission track thermochronology in the Scott Glacier region. *Journal of Geophysical Research* **102(B4)**, 7747–7765.

Fitzgerald, P. G., Sandiford, M., Barrett, P. J. & Gleadow, A. J. W. (1987). Asymmetric extension associated with uplift and subsidence in the Transantarctic Mountains and Ross Sea Embayment. *Earth and Planetary Science Letters* **81**, 67–78.

Francis, D. M. (1976). The origin of amphibole in lherzolite xenoliths from Nunivak Island, Alaska. *Journal of Petrology* **17**, 357–378, doi:10.1093/petrology/17.3.357.

Frey, F. A. (1980). The origin of pyroxenites and garnet pyroxenites from Salt Crater, Oahu, Hawaii; trace element evidence. *American Journal of Science* **280A**, 427–449.

Frey, F. A. & Prinz, M. (1978). Ultramafic inclusions from San Carlos, Arizona; petrologic and geochemical data bearing on their petrogenesis. *Earth and Planetary Science Letters* **38**, 129–176.

Gamble, J. A. & Kyle, P. R. (1987). The origin of glass and amphibole in spinel-wehrlite xenoliths from Foster Crater, McMurdo Volcanic group, Antarctica. *Journal of Petrology* **28**, 755–779.

Gamble, J. A., McGibbon, F., Kyle, P. R., Menzies, M. A. & Kirsch, I. (1988). Metasomatized xenoliths from Foster Crater, Antarctica: implications for lithosphere structure and processes beneath the Transantarctic Mountains. *Journal of Petrology, Special Lithosphere Issue* 109–138.

Ghiorso, M. S., Hirschmann, M. M., Reiners, P. W. & Kress, V. C. (2002). The pMELTS: a revision of MELTS for improved calculation of phase relations and major element partioning related to partial melting for the mantle to 3GPa. *Geochemistry, Geophysics, Geosystems* **3**, doi:10.1029/2001GC00217.

Green, D. H. & Falloon, T. J. (1998). Pyrolite: a Ringwood concept and its current expression. In: Jackson, I. (ed.) *The Earth's Mantle: Composition, Structure and Evolution, 7.* Cambridge: Cambridge University Press, pp. 311–378.

Gregory, R. & Taylor, H. (1986). Non-equilibrium, metasomatic $^{18}O/^{16}O$ effects in upper mantle mineral assemblages. *Contributions to Mineralogy and Petrology* **93**, 124–135.

Griffin, W. L., Wass, S. Y. & Hollis, J. D. (1984). Ultramafic xenoliths from Bullenmerri and Gnotuk maars, Victoria, Australia; petrology of a sub-continental crust–mantle transition. *Journal of Petrology* **25**, 53–87.

Halliday, A. N., Lee, D. C., Tommasini, S., Davies, G. R. & Paslick, C. R. (1995). Incompatible trace elements in OIB and MORB and source enrichment in the sub-oceanic mantle. *Earth and Planetary Science Letters* **133**, 379–395.

Hirschmann, M. M. & Stolper, E. M. (1996). A possible role for garnet pyroxenite in the origin of the 'garnet signature' in MORB. *Contributions to Mineralogy and Petrology* **124**, 185–208.

Ho, K., Chen, J., Smith, A. D. & Juang, W. (2000). Petrogenesis of two groups of pyroxenite from Tungchihsu, Penghu Islands, Taiwan Strait: implications for mantle metasomatism beneath SE China. *Chemical Geology* **167**, 355–372.

Hofmann, A. W. (1997). Mantle geochemistry: the message from oceanic volcanism. *Nature* **385**, 219–229.

Hornig, I., Wörner, G. & Zipfel, J. (1991). Lower crustal and mantle xenoliths from Mt. Melbourne Volcanic Field, Northern Victoria Land, Antarctica. *Memorie della Società Geologica Italiana* **46**, 337–352.

Irvine, T. N. & Baragar, W. R. A. (1971). A guide to the chemical classification of the common volcanic rocks. *Canadian Journal of Earth Sciences* **8**, 523–548.

Irving, A. J. (1974). Geochemical and high pressure experimental studies of garnet pyroxenite and pyroxene granulite xenoliths from the Delegate basaltic pipes, Australia. *Journal of Petrology* **15**, 1–40.

Irving, A. J. (1980). Petrology and geochemistry of composite ultramafic xenoliths in alkalic basalts and implications for magmatic processes within the mantle. *American Journal of Science* **280A**, 389–426.

Irving, A. J. & Frey, F. A. (1984). Trace element abundances in megacrysts and their host basalts; constraints on partition coefficients and megacryst genesis. *Geochimica et Cosmochimica Acta* **48**, 1201–1221.

Kyle, P. R. (1990). McMurdo Volcanic Group—Western Ross Embayment: Introduction. In: LeMasurier, W. E. & Thomson, J. W. (eds) *Volcanoes of the Antarctic Plate and Southern Oceans*. Washington, DC: American Geophysical Union Washington, pp. 19–25.

Kyser, T. K. (1990). Stable isotopes in the continental lithospheric mantle. In: Menzies, M. (ed.) *The Continental Lithosphere*. Oxford: Clarendon Press, pp. 127–156.

Leake, B. E., Woolley, A. R., Arps, C. E. S. *et al.* (1997). Nomenclature of amphiboles: Report of the subcommittee on amphiboles of the International Mineralogical Association, commission on new minerals and mineral names. *Canadian Mineralogist* **35**, 219–246.

Le Bas, M. J., Le Maitre, R. W., Streckeisen, A. & Zanettin, R. (1986). A chemical classification of volcanic rocks based on total alkali–silica diagram. *Journal of Petrology* **27**, 745–750.

LeMasurier, W. E. & Thomson, J. W. (1990). *Volcanoes of the Antarctic Plate and Southern Oceans. American Geophysical Union, Antarctic Research Series* **18**, , 487 p.

Lindsley, D. H. (1983). Pyroxene thermometry. *American Mineralogist* **68**, 477–493.

Mattey, D., Lowry, D. & Macpherson, C. (1994). Oxygen isotope composition of mantle peridotite. *Earth and Planetary Science Letters* **128**, 231–241.

McDonough, W. F. & Sun, S.-s. (1995). The composition of the Earth. *Chemical Geology* **120**, 223–253.

McGinnis, L. D., Bowen, R. H., Erickson, J. M., Allred, B. J. & Kreamer, J. L. (1985). East–west Antarctic boundary in McMurdo Sound. *Tectonophysics* **114**, 341–356.

Menzies, M. A., Kempton, P. & Dugan, M. (1985). Interaction of continental lithosphere and asthenospheric melts below the Geronimo Volcanic Field, Arizona, U.S.A. *Journal of Petrology* **26**, 663–693, doi:10.1093/petrology/26.3.663.

Michael, P. J. (1988). The concentration, behavior and storage of H_2O in the suboceanic upper mantle—implications for mantle metasomatism. *Geochimica et Cosmachimica Acta* **52**, 555–566.

Muller, P., Schmidt-Tomè, M., Kreuzer, H., Thessensohn, F. & Vetter, U. (1991). Cenozoic peralkaline magmatism at the western Margin of the Ross Sea, Antarctica. *Memorie della Società Geologica Italiana* **46**, 315–336.

Nardini, I., Armienti, P., Rocchi, S., Dallai, L. & Harrison, D. (2009). Sr–Nd–Pb–He–O isotope and geochemical constraints to the genesis of Cenozoic magmas from the West Antarctic rift. *Journal of Petrology* **50**, 1359–1375.

Nimis, P. (1999). Clinopyroxene geobarometry of magmatic rocks. Part 2. Structural geobarometers for basic to acid, tholeiitic and mildly alkaline magmatic systems. *Contributions to Mineralogy and Petrology* **135**, 62–74.

Nimis, P. & Ulmer, P. (1998). Clinopyroxene geobarometry of magmatic rocks: Part 1. An expanded structural geobarometer for anhydrous and hydrous, basic and ultrabasic systems. *Contributions to Mineralogy and Petrology* **133**, 122–135.

O'Hara, M. J. (1968). The bearing of phase equilibria studies in synthetic and natural systems on the origin and evolution of basic and ultrabasic rocks. *Earth-Science Reviews* **4**, 69–133.

Orlando, A., Armienti, P., Conticelli, S., Vagelli, G. & Manetti, P. (1997). Petrologic investigations on the primitive Cainozoic lavas of Northern Victoria Land, Antarctica. In: Ricci, C. A. (ed.) *The Antarctic Region: Geological evolution and processes*. Siena: Terra Antartica, pp. 523–530.

Orlando, A., Conticelli, S., Borrino, D. & Armienti, P. (2000). Experimental study on a primary basanite from McMurdo Volcanic Group, Antarctica: Inference on its mantle source. *Antarctic Science* **12(1)**, 105–116.

Perinelli, C., Armienti, P. & Dallai, L. (2006). Geochemical and O-isotope constraints on the evolution of lithospheric mantle in the Ross Sea rift area (Antarctica). *Contributions to Mineralogy and Petrology* **151**, 245–266.

Perinelli, C., Orlando, A., Conte, A. M., Armienti, P., Borrini, D., Faccini, B. & Misiti, V. (2008). Metasomatism induced by alkaline magma on upper mantle of the Northern Victoria Land (Antarctica): an experimental approach. In: Coltorti, M. & Grégoire, M. (eds) *Mantle Metasomatism in Intra-plate and Suprasubduction Settings. Geological Society, London, Special Publications* **293**, 197–221, doi:10.1144/SP293.10.

Perkins, G. B., Sharp, Z. D. & Selverstone, J. (2006). Oxygen isotope evidence for subduction and rift-related mantle metasomatism beneath the Colorado Plateau–Rio Grande rift transition. *Contributions to Mineralogy and Petrology* **151**, 633–650.

Pike, J. E. N. & Schwarzman, F. C. (1977). Classification of textures in ultramafic xenoliths. *Journal of Geology* **85**, 49–61.

Pilet, S., Hernandez, J., Bussy, F. & Sylvester, P. J. (2004). Short-term metsomatic control of Nb/Th ratios in the mantle sources of intraplate basalts. *Geology* **32**, 113–116.

Pilet, S., Baker, M. B. & Stolper, E. M. (2008). Metasomatized lithosphere and origin of alkaline lavas. *Science* **320**, 916–919, doi:10.1126/science.1156563.

Putirka, K. D. (2008). Thermometers and barometers for volcanic systems. In: Putirka, K. D. & Tepley, F. J., III (eds) *Minerals, Inclusions and Volcanic Processes. Mineralogical Society of America and Geochemical Society, Reviews in Mineralogy and Geochemistry* **69**, 61–120.

Putirka, K. D. & Condit, C. D. (2003). Cross section of a magma conduit system at the margin of the Colorado Plateau. *Geology* **31**, 701–704.

Putirka, K. D., Mikaelian, H., Reyerson, F. & Shaw, H. (2003). New clinopyroxene–liquid thermobarometers for mafic, evolved, and volatile-bearing lava compositions, with applications to lavas from Tibet and the Snake River Plain, Idaho. *American Mineralogist* **88**, 1542–1554.

Rocchi, S., Armienti, P., D'Orazio, M., Tonarini, S., Wijbrans, J. & Di Vincenzo, G. D. (2002). Cenozoic magmatism in the western Ross Embayment: role of mantle plume vs plate dynamics in the development of the West Antarctic Rift System. *Journal of Geophysical Research* **107(B7),** doi:10.1029/2001JB000515.

Rocchi, S., Storti, F., Di Vincenzo, G. & Rossetti, F. (2003). Intraplate strike-slip tectonics as an alternative to mantle plume activity for the Cenozoic rift magmatism in the Ross Sea region, Antarctica. In: Storti, F., Holdsworth, R. E. & Salvini, F. (eds) *Intraplate Strike-Slip Deformation Belts. Geological Society, London, Special Publications* **210**, 145–158.

Rocchi, S., Armienti, P. & Di Vincenzo, G. (2005). No plume, no rift magmatism in the West Antarctic Rift. In: Foulger, G. R., Natland, J. H., Presnall, D.C. & Anderson, D. L. (eds) *Plates, Plumes, and Paradigms. Geological Society of America, Special Papers* **388**, 435–447.

Rocholl, A., Stein, M., Molzahn, M., Hart, S. R. & Wörner, G. (1995). Geochemical evolution of rift magmas by progressive trapping of a stratified mantle source beneath the Ross Sea Rift, Northern Victoria Land, Antarctica. *Earth and Planetary Science Letters* **131**, 207–224.

Roeder, P. L. & Emslie, R. F. (1970). Olivine–liquid equilibrium. *Contributions to Mineralogy and Petrology* **29**, 275–289.

Rosenbaum, J. M., Walker, D. & Kyser, T. K. (1994). Oxygen isotope fractionation in the mantle. *Geochimica et Cosmochimica Acta* **58**, 4767–4777.

Salvini, F., Brancolini, G., Busetti, M., Storti, F., Mazzarini, F. & Coren, F. (1997). Cenozoic geodynamics of the Ross Sea region of Antarctica: Crustal extension, intraplate strike-slip faulting and tectonic inheritance. *Journal of Geophysical Research* **102**, 24669–24696.

Sharp, Z. D. (1995). Oxygen isotope geochemistry of the Al_2SiO_5 polymorphs. *American Journal of Science* **295**, 1058–1076.

Simons, K., Dixon, J., Schilling, J.-G., Kingsley, R. & Poreda, R. (2002). Volatile in basaltic glasses from the Easter–Salas y Gomez Seamount Chain and Easter Microplate: Implications for geochemical recycling of volatile elements. *Geochemistry, Geophysics, Geosystems* **3**, doi:10.1029/2001GC000173.

Skulski, T., Minarik, W. & Watson, E. B. (1994). High-pressure experimental trace-element partitioning between clinopyroxene and basaltic melts. *Chemical Geology* **117**, 127–147.

Stagg, H. M. J. & Willcox, J. B. (1992). A case for Australia–Antarctica separation in the Neocomian (*ca.* 125 Ma). *Tectonophysics* **210**, 21–32.

Storti, F., Salvini, F., Rossetti, F. & Phipps Morgan, J. (2007). Intraplate termination of transform faulting within the Antarctic continent. *Earth and Planetary Science Letters* **260**, 115–126.

Suen, C. J. & Frey, F. A. (1987). Origins of the mafic and ultramafic rocks in the Ronda Peridotite. *Earth and Planetary Science Letters* **85**, 183–202.

Tessensohn, F. & Wörner, G. (1991). The Ross Sea Rift System (Antarctica): Structure, evolution and analogues. In: Thomson, M. R. A., Crame, J. A. & Thomson, J. W. (eds) *Geological Evolution of Antarctica*. Cambridge: Cambridge University Press, pp. 273–277.

Tonarini, S., Rocchi, S., Armienti, P. & Innocenti, F. (1997). Constraints on timing of Ross Sea rifting inferred from Cainozoic intrusions from Northern Victoria Land, Antarctica. In: Ricci, C. A. (ed.) *The Antarctic Region: Geological Evolution and Processes*. Siena: Terra Antartica, pp. 511–522.

Trehu, A., Holt, T., Behrendt, J. C. & Fritsch, J. (1989). Crustal structure in the Ross Sea, Antarctica: preliminary results from GANOVEX V. *EOS Transactions, American Geophysical Union* **43**(Supplements 70), 1344.

Turcotte, D. L. & Schubert, G. (2002). *Geodynamics*. New York: Cambridge University Press, 456 p.

Wilshire, H. G. & Shervais, J. W. (1975). Al-augite and Cr-diopside ultramafic xenoliths in basaltic rocks from western United States. *Physics and Chemistry of the Earth* **9**, 257–272.

Wörner, G. (1999). Lithospheric dynamics and mantle sources of alkaline magmatism of the Cenozoic West Antarctic Rift System. *Global and Planetary Change* **23**, 61–77.

Wulff-Pedersen, E., Neumann, E.-R., Vannucci, R., Bottazzi, P. & Ottolini, L. (1999). Silicic melts produced by reaction between peridotite and infiltrating basaltic melts: ion probe data on glasses and minerals in veined xenoliths from La Palma, Canary Islands. *Contributions to Mineralogy and Petrology* **137**, 59–82.

Xia, Q., Dallai, L. & Deloule, E. (2004). Oxygen and hydrogen isotope heterogeneity of clinopyroxene megacrysts from Nushan Volcano, SE China. *Chemical Geology* **209**, 137–151.

Zajacz, Z., Kovács, I., Szabó, C., Halter, W. & Pettke, T. (2007). Evolution of mafic alkaline melts crystallized in the uppermost lithospheric mantle: a melt inclusion study of olivine–clinopyroxenite xenoliths, northern Hungary. *Journal of Petrology* **48**, 853–883.

Zhang, H. F., Menzies, M. A., Mattey, D. P., Hinton, R. W. & Gurney, J. J. (2001). Petrology, mineralogy and geochemistry of oxide minerals in polymict xenoliths from the Bultfontein kimberlites, South Africa: implication for low bulk-rock oxygen isotopic ratios. *Contributions to Mineralogy and Petrology* **141**, 367–379.

Zhao, Z.-F. & Zheng, Y. F. (2003). Calculation of oxygen isotope fractionation in magmatic rocks. *Chemical Geology* **193**, 59–80.

Zheng, Y. F. (1993). Calculation of oxygen isotope fractionation in anhydrous silicate minerals. *Geochimica et Cosmochimica Acta* **57**, 1079–1091.

Zindler, A. & Hart, S. R. (1986). Helium: problematic primordial signals. *Earth and Planetary Science Letters* **79**, 1–8.

Zipfel, J. & Wörner, G. (1992). Four- and five-phase peridotites from a continental rift system: evidence for upper mantle uplift and cooling at the Ross Sea margin (Antarctica). *Contributions to Mineralogy and Petrology* **111**, 24–36.